

2 **Doping liquid argon with xenon in ProtoDUNE** 3 **Single-Phase**

4 **D.L. Adams, M.C.Q. Bazetto, L. Bomben, S. Bordoni, F. Boran, C. Brizzolari, G. Brunetti, C.**
5 **Cattadori, F. Cavanna, G. De Souza, F. Dolek, Z. Djurcic, A. Falcone, N. Gallice, A. Himmel, U.**
6 **Kose, E. Lutsenko, A.A. Machado, F. Pietropaolo, M. Prest, A. Rafique, B. Ramson, F.**
7 **Resnati, P. Sala, E. Segreto, K. Spurgeon, H. Vieira de Souza, D. Totani, S. Tufanli, E.**
8 **Vallazza, D. Warner, D. Whittington, R.J. Wilson, A. Zani**

9 ABSTRACT: Doping of liquid argon TPCs (LArTPC) with a small concentration of xenon is a well-
10 known technique for light-shifting and eases the detection of the liquid argon scintillation light. In
11 this paper, we present the results of the first doping test ever performed in a kton scale LArTPC.
12 From February to May 2020, we carried out this special run in the DUNE Single Phase ProtoDUNE
13 prototype (ProtoDUNE-SP) at CERN, featuring a mass of 770 tons of liquid argon (fiducial: 400
14 tons). The goals of the run were to measure the light and charge response of the detector to
15 xenon up to a concentration of 20 ppm, reduce the non-uniformities in light collection caused by
16 the location of the DUNE photosensors in the anode only, and compensate for light losses due
17 to air contamination. Light collection was analysed as a function of the xenon concentration, by
18 using the ProtoDUNE Photon Detection System (PDS) and a dedicated setup installed before the
19 run. In this paper we review the physics of xenon doping and the injection method deployed in
20 ProtoDUNE-SP. Then, we discuss the obtained results, which demonstrate a successful procedure.
21 We are able to disentangle argon and xenon light intensity and measure their dependence on the
22 dopant concentration; we perform studies of the collection efficiency as a function of the distance
23 between tracks and light detectors, obtaining enhanced uniformity of response. Incidentally, we
24 show that xenon doping can help recovering from light losses due to contamination of the liquid
25 argon.

26 **KEYWORDS:** Noble liquid detectors (scintillation, ionization, double-phase); Neutrino detectors

27 **Contents**

28	1 Introduction	2
29	2 Xenon doping of liquid argon	3
30	2.1 Xenon basic properties	3
31	2.2 Doping liquid argon with xenon and its advantages	3
32	2.3 Principles of xenon doping in LAr	4
33	2.4 Effect of nitrogen contamination in LAr	5
34	3 The ProtoDUNE Single-Phase detector	6
35	3.1 Photon Detection System	6
36	3.2 Cosmic-Ray Tagger	7
37	3.3 The X-ARAPUCA detectors in ProtoDUNE-SP	8
38	4 Cryogenics operations for xenon doping in ProtoDUNE-SP	10
39	4.1 Nitrogen contamination	11
40	4.2 Xenon doping campaign of ProtoDUNE SP	11
41	5 Analysis of the X-ARAPUCA data	12
42	5.1 Data selection and deconvolution	13
43	5.2 Effects of xenon on LAr light	14
44	6 Analysis of the ProtoDUNE-SP PDS	19
45	6.1 Triggering, data selection, and collected light	19
46	6.2 Light recovery due to xenon injection	20
47	7 Charge reconstruction in liquid argon doped with xenon	26
48	8 Conclusions - NOT CORRECTED YET	27
49	A Details on xenon injections in ProtoDUNE SP and contaminations	29

1 Introduction

Liquid Argon Time Projection Chambers (LArTPC, [1]) are prominent in contemporary physics for the study of neutrino oscillations and the search for rare events, including Dark Matter [2–5]. This technology has been developed for more than 40 years and reached a level of sophistication scalable up to multi-kilotonnes detectors. DUNE, in particular, is designing and constructing four underground modules with a total mass of 17 kt each, which will be located at the Sanford Underground Research Facility (SURF) in South Dakota, USA. Its main goal is the precise determination of neutrino oscillation parameters, which will be achieved mainly with beam neutrinos; other than that, atmospheric, supernovae and solar neutrino detection, as well as proton decay and Beyond the Standard Model (BSM) physics searches, are planned [6, 7]. A LArTPC exploits the deposited ionization charge in argon, drifted towards the anode plane, to perform spatial and calorimetric reconstruction of events. Furthermore, liquid argon (LAr) is a high-performance scintillator. It emits light in the Vacuum UltraViolet (VUV) region with a spectrum centered at $\lambda = 128$ nm and a yield of about 4×10^4 (2.4×10^4) photons/MeV at 0 V/cm (500 V/cm) electric field. The scintillation light is produced by de-excitation of the singlet ($\tau_s \simeq 6$ ns) and triplet ($\tau_t \simeq 1.3$ μ s) states of the unstable excited dimer Ar_2^* ; their ratio depends on the energy loss mechanism and can be used for particle identification by the analysis of the pulse shape.

Detecting VUV light in liquid argon is challenging but the physics advantages are remarkable, especially in DUNE. The scintillation light provides the t_0 to the TPC and the third coordinate of the interaction. It then improves by one order of magnitude (1 cm \rightarrow 1 mm) the localization of the interaction vertex, with respect to the t_0 provided by the proton kicker of the neutrino beam (LBNF for DUNE). Furthermore, light collection is the main tool to trigger events that are not produced by the beam and plays a special role in triggering and recording supernovae neutrino bursts. The light is also anti-correlated with the ionization loss of the particle and can be exploited for combined charge-light calorimetry. A high light collection efficiency can outperform the TPC energy resolution, especially for low energy events [8].

The DUNE Photon Detection System (PDS) can be enhanced by doping LAr with xenon at the level of few tens of ppm¹. DUNE is exploring this opportunity because the longer Rayleigh scattering length of the shifted light in LAr should increase the light collection far from the photon detectors. Furthermore, the xenon emission can be collected with higher efficiency due to its longer wavelength. Previous literature studies ([9–13]) have demonstrated the doping procedure on small scale detectors, and sometimes in gas phase. In order to test the feasibility of such operation in DUNE, it is necessary to perform it at an intermediate scale: therefore, a dedicated xenon doping run was performed with the 770 t Single Phase DUNE ProtoType at CERN (ProtoDUNE Single-Phase, SP) [14, 15] in 2020, which represents a new milestone in the development of very-large-volume LArTPCs.

The ProtoDUNE-SP PDS was enhanced with the addition of two prototypes of X-ARAPUCA photon detectors, i.e. the technology that was selected for deployment in the first module of the DUNE Far Detector (called FD1).

¹In this paper, unless otherwise specified, the fractional amounts ppm, ppb, ppt (parts per million/billion/trillion) are to be intended as expressing fractions of *mass*.

89 In this paper, we describe the preparation and the results of the xenon doping run of ProtoDUNE-
90 SP, obtained both with the X-ARAPUCA and the standard PDS. Physics of xenon-doped liquid
91 argon is introduced in Section 2; ProtoDUNE-SP and its Photon Detection System is described in
92 Section 3, after which the actual xenon doping procedure is detailed 4. The analysis of the data
93 recorded by the X-ARAPUCA is presented in Section 5; the studies performed with the main PDS
94 are instead shown in Section 6. Finally, we used the TPC of ProtoDUNE-SP to evaluate the effect
95 of the xenon presence on the charge collection, as discussed in Section 7.

96 2 Xenon doping of liquid argon

97 In order to enhance the response of the DUNE PDS, the DUNE Collaboration has been considering
98 the possibility of doping liquid argon with xenon, mainly due to the more favourable physical
99 properties of its scintillation light: these have been investigated in literature on a number of smaller
100 detectors over the years (see for instance [9–13]).

101 2.1 Xenon basic properties

102 Xenon is a noble cryogenic liquid as argon and it is exploited in various direct Dark Matter search
103 experiments [16, 17]. Indeed, it has more favorable properties with respect to argon (e.g. higher
104 density, atomic number and electron mobility), that make it appealing as primary target/detecting
105 medium in dual-phase TPCs for Dark Matter searches. On the other hand, due to its low availability
106 and high production cost, its use in particle physics is quite limited.

107 Xenon liquefies at 165 K and freezes at 161 K. It is a high-yield scintillator as argon: the
108 average energy needed to produce a scintillation photon in xenon is slightly lower than that of
109 argon, for both low- and high-ionization density particles [18]: this results in a slightly higher
110 photon yield ($> 4.2 \times 10^4$ photons/MeV without electric field). Xenon scintillation light is emitted
111 at 178 nm, still in the Ultra-Violet (UV) but in a region where commercial photo-detectors are
112 reasonably sensitive (see below). It features two components, as argon, both much faster than the
113 argon triplet light (4 and 22 ns).

114 2.2 Doping liquid argon with xenon and its advantages

115 Converting liquid argon scintillation light to a larger wavelength has significant advantages in a
116 LArTPC, especially if the shift can be performed uniformly within the drift volume, instead than on
117 the photo-sensitive devices (as it happens for standard wavelength-shifting, WLS, coatings). At the
118 xenon wavelength (178 nm), light detectors with high enough sensitivity are already commercially
119 available (both PMTs and SiPMs). For example, the PDE of last-generation SiPMs at that wavelength
120 exceeds 25% (citation). This would ensure quite efficient collection of the xenon light, allowing the
121 removal of further wavelength-shifting elements, like Tetra-Phenyl Butadiene (TPB).

122 Furthermore, the faster de-excitation decay time constants of xenon (4 and 22 ns), with respect
123 to argon, contributes to faster pulse profiles. Even considering the convolution of the various
124 processes involved in argon-xenon excitation transfer, one can obtain signals with an overall decay
125 constant of few hundreds ns. Finally, the Rayleigh scattering length in liquid argon at 178 nm
126 is significantly larger than that at 128 nm. This is largely due to the fact that argon refraction
127 index n is rapidly decreasing in the Ultra-Violet region of the spectrum, as a function of increasing

128 wavelength [19]. In the framework of an experiment like DUNE, with very large drift distances
129 involved, this should help obtaining a more uniform response, in terms of photons reaching the
130 light detectors, as a function of the distance from the detectors themselves. In turn, this will
131 allow enhancing the detection efficiency for low energy events (not beam-related) far from the light
132 detectors.

133 The mentioned properties of xenon make it the more appealing for use as a dopant in the DUNE
134 LAr-TPCs, the larger the drift distance. The present plan is to employ it in a LArTPC geometry
135 different from the one of ProtoDUNE-SP, i.e., a vertical drift TPC with a 6 m drift that will be
136 installed ad DUNE Far Detector 2 (FD2, [20]).

137 2.3 Principles of xenon doping in LAr

138 As xenon solidifies at 161 K, its dilution in argon must be performed with extreme care, in order
139 to avoid its freezing. Usually, its concentration in previous experiments ranges from few ppm to
140 few %, with light shifting effects setting on already at the few ppm level (citation). According
141 to present models (citation), xenon atoms in suspension in liquid argon interfere with the light
142 production process that involves the argon excited dimers Ar_2^* . Dimers might form in two states,
143 a singlet one $^1\Sigma_u^+$ characterized by a fast decay constant (6 ns, thus dubbed in the following “fast
144 component”), and a triplet state $^3\Sigma_u^+$ with a much larger decay time (~ 1300 ns, “slow component”).

145 As shown in Figure 1, in the presence of xenon, a non-radiative collision of a first xenon atom
146 with the dimer leads to the formation of a new hybrid dimer ArXe^* , whereas the interaction of a
147 second Xe atom yields a full transfer of energy to a Xe_2^* dimer, which is at this point the entity
148 decaying with emission of light, at 178 nm. The time constants of these two transition processes
149 are identified in Figure 1 as τ_{AX} and τ_{XX} , and they depend directly on the xenon concentration.
150 At relatively low concentrations, below 1 ppm, the double interaction has a low enough probability
151 to let a certain number of hybrid dimers ArXe^* survive long enough to de-excite, producing an
152 intermediate light component around 150 nm [21]. This hybrid component is expected to disappear
153 as the concentration increases to few ppm.

154 The effect of xenon doping on the collected scintillation light is mainly that the number of
155 photons emitted from the long-lived triplet state of the Ar_2^* dimer ($^3\Sigma_u^+$) drops significantly, as the
156 dimer is destroyed by the collision with xenon atoms. Overall, the total light emitted is characterised
157 by smaller decay-time constants, given by the presence of xenon. The characteristic time profile of
158 the liquid argon scintillation pulse is modified by the presence of xenon, in a way that is proportional
159 to its concentration. This effect will be illustrated in more detail when discussing the data collected
160 in ProtoDUNE SP in Sections 5 and 6.

161 According to literature(e.g. [22] and references therein), the presence of few ppm of xenon
162 in LAr is sufficient to shift a significant portion of 128 nm LAr photons to xenon scintillation
163 wavelength. In a detector like ProtoDUNE-SP, this translates into injecting few kg of xenon in the
164 LAr bulk: for this reason, it was deemed feasible and important to use the detector as a test-bed for
165 the study of the effects of xenon-doping at large scale. It is worth noting that doping such a large
166 detector has never been attempted before and the long-term behaviour of xenon in LAr was never
167 investigated at this scale.

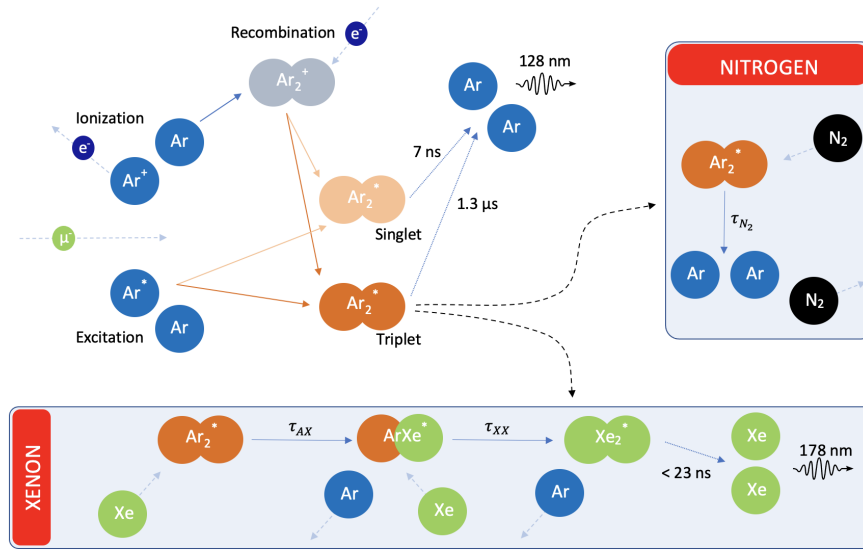


Figure 1: Schematic representation of the production process of scintillation light in pure liquid argon, with concurrent effects nitrogen quenching and xenon doping. The time constants of the non-radiative energy-transfer processes τ_{AX} and τ_{XX} depend on the xenon concentration in LAr.

168 2.4 Effect of nitrogen contamination in LAr

169 As discussed in [23], the presence of nitrogen in liquid argon affects scintillation light emission. This
 170 is a well-known process called quenching, where the non-radiative collisional reaction $Ar_2^* + N_2 \rightarrow$
 171 $2Ar + N_2$ destroys the argon triplet excimers before de-excitation.

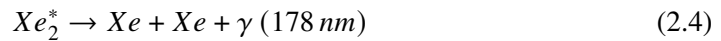
172 Given the characteristics of the xenon interaction with the long-lived triplet state argon dimers,
 173 this process can be competitive with the mentioned light quenching [22]. Indeed, it appears to have
 174 a larger interaction cross-section, with respect to quenching. For this reason, while introducing its
 175 own advantages to scintillation light collection, xenon doping can also help in negating the effects
 176 of pollutants in liquid argon, recovering light that would otherwise be lost. This was the case
 177 for ProtoDUNE-SP, which experienced an unexpected accident with an argon recirculation pump,
 178 introducing a non-negligible amount of nitrogen in the liquid bulk (see Section 4.1).

179 In the ternary mixture Ar-N₂-Xe, the concurrent processes below are expected, schematised in
 180 Figure 1:

- 181 • Ar_2^* dimers would normally decay to 2 Ar atoms by emitting light at 128 nm, with the usual
 182 two very different decay times already mentioned;
- 183 • If a quencher like N₂ is present in the liquid, non-radiative interactions with the quencher can
 184 cause dimer destruction, without light emission [23]. The most affected species is the Ar_2^*
 185 triplet state $^3\Sigma_u^+$, due to its very large life-time;
- 186 • if xenon is also present in LAr, its non-radiative interactions with the long-lived triplet states
 187 of Ar_2^* become concurrent with those due to nitrogen, and can lead to the formation of mixed
 188 excited state $ArXe^*$;

- 189 • according to the concentration of xenon (up to around 1 ppm), a fraction of $ArXe^*$ molecules
190 will de-excite, emitting a characteristic 150 nm radiation [21]. The rest (all of them at higher
191 concentrations) will interact again with single xenon atoms, producing Xe_2^* dimers that will
192 then decay emitting 178 nm photons,
- 193 • nitrogen can in principle affect all the reactions mentioned above, but the time scales of all
194 those interactions involving xenon are short enough to be less affected by nitrogen itself.

195 A more detailed discussion about the modelization of the ternary mixture and its characteriza-
196 tion in large volume LArTPCs is deferred to a later publication



197 3 The ProtoDUNE Single-Phase detector

198 The ProtoDUNE single-phase LArTPC (ProtoDUNE-SP) is a full scale prototype for the first
199 module of the DUNE FD1 [7]. With a total LAr mass of 0.77 kt, it is the largest single-phase
200 LArTPC detector built to date. It is located in the dedicated extension of the EHN1 hall in CERN
201 North Area, where a tertiary portion was added to the existing H4 beam-line, to provide very low-
202 energy charged-particle beams, as part of the CERN Neutrino Platform program. Construction,
203 installation and commissioning of ProtoDUNE-SP detector was completed in July 2018, and is
204 reported in [14]. Immediately after LAr filling and detector activation, beam data were collected in
205 the 0.3-7 GeV range from September to November 2018 [15]. After the beam run, it operated until
206 July 2020 collecting data with cosmics, to validate the design solutions for the future DUNE far
207 detector modules, demonstrate operational stability, and eventually to perform R&D on different
208 aspects of LArTPC technology. Doping LAr with xenon to enhance the light collection of the
209 photon detectors, as presented in this paper, was part of such an R&D effort: an extended test was
210 performed during the last six months before the end of operations of ProtoDUNE-SP.

211 ProtoDUNE-SP TPC has 411 tons of active LAr volume with dimensions of 6.0 m \times 6.9 m \times
212 7.2 m. As shown in Fig. 2, the active volume is split in two by a central cathode plane, defining
213 two identical volumes, with 3.6 m of drift length. The cathode is biased to -180 kV, providing a
214 uniform 500 V/cm electric field in the drift region. On both sides of the cathode, at a distance of
215 3.6 m, the anode planes assemblies (APAs) are installed. Each APA is made up of four layers of
216 wire planes (three active + a grid layer) for charge readout. Each drift volume is read-out by three
217 APAs. The two volumes are called Left chamber and Right chamber, according to their position
218 along the direction of the incoming charged-particle beam.

219 3.1 Photon Detection System

220 Photons produced by LAr scintillation are recorded by the photon detection system (PDS) modules,
221 which is made of 60 optical modules of active area 207 \times 8.6 cm each. 10 modules are inserted

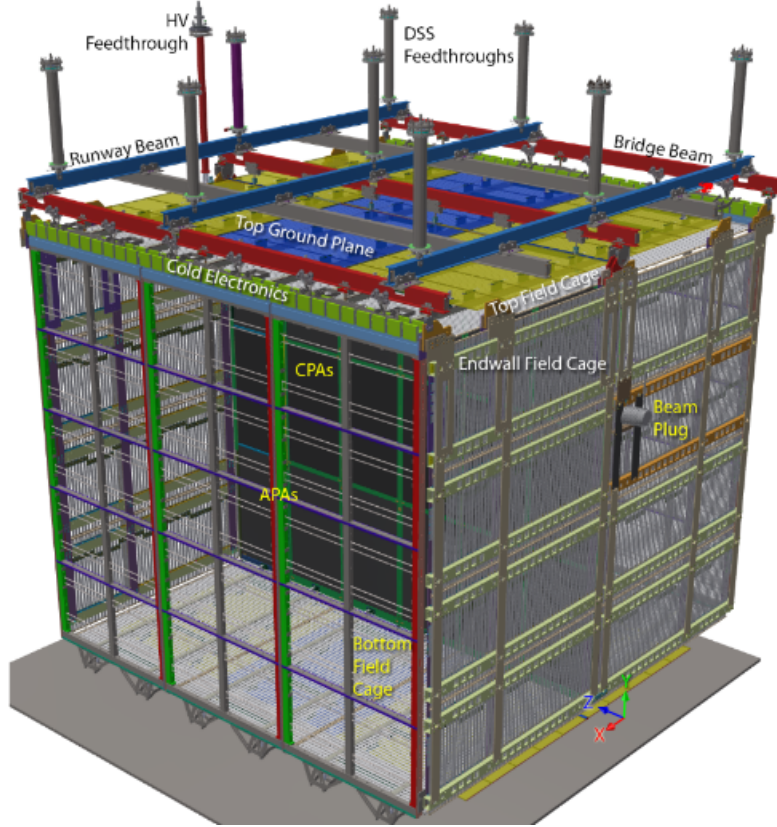


Figure 2: 3D model of the ProtoDUNE-SP detector with labelling of all major components.

222 into each APA frame, regularly spaced along the vertical direction. Each module combines a
 223 photon collector and a photon sensor. Three different collector designs were implemented in
 224 ProtoDUNE-SP: “double-shift light guides” [24], “dip-coated light guides” [25, 26], and ARAPUCA
 225 light traps [27]. Silicon Photomultiplier (SiPM) arrays from Hamamatsu and SensL vendors are
 226 deployed as sensors. The location of PDS modules in an APA frame and the three types of detector
 227 technologies are shown in Figure 3. The PDS performance is illustrated in detail in [14, 15].

228 3.2 Cosmic-Ray Tagger

229 The ProtoDUNE-SP detector is exposed to a flux of ~ 180 cosmic muons/(m^2 s). A fraction of
 230 these particles is tagged by a Cosmic-Ray Tagger (CRT, [14]): this is made of scintillator counters
 231 (strips) read by Silicon PhotoMultipliers, and it consists of four large assemblies, two mounted
 232 upstream and two downstream of the cryostat. Each assembly covers an area approximately 6.8 m
 233 high and 3.65 m wide. Modules are instrumented with 64 scintillator strips 5 cm wide and 365
 234 cm long. Two-dimensional sensitivity is achieved by putting together groups of four modules into
 235 assemblies, with two modules being rotated by 90° with respect to the other two. It is then possible
 236 to reconstruct a muon track through the CRT, by drawing a line from hits in the upstream modules
 237 to hits in the downstream modules, the muon time-of-flight information dictating the width of the
 238 relative coincidence window. For the purposes of the ProtoDUNE detector studies, this allows

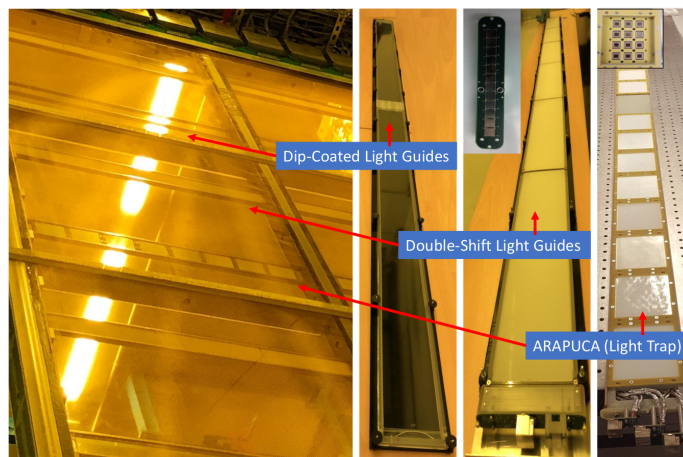


Figure 3: The three technologies of PDS modules shown inside the APA frame and on desk for comparison.

239 selecting uniform sets of cosmic-ray muons parallel to APAs, with a well defined direction and time
 240 stamp.

241 3.3 The X-ARAPUCA detectors in ProtoDUNE-SP

242 The ARAPUCA technology is based on light trapping, as discussed in [27]. In the base concept,
 243 trapping of 128 nm photons is achieved as follows: 128 nm photons hitting the detector are shifted
 244 down to 350 nm by a p-terphenyl (pTp) coating located on top of a dichroic filter, that features a
 245 400 nm transparency cutoff. A second coating layer, with Tetraphenyl Butadiene (TPB), converts
 246 350 nm photons to 420 nm. The upgrade of the technology (X-ARAPUCA) replaces the second
 247 coating layer with a WLS light guide, enhancing photon collection efficiency. [28]. In both versions,
 248 the obtained 420 nm photons are trapped inside the detector by the filter, fully reflective above the
 249 400 nm cutoff, and they bounce back-and-forth until they reach the photosensors (cryogenic SiPMs).

250 Two ARAPUCA modules were installed in ProtoDUNE-SP for the first beam run, and they came
 251 out to be the preferred technology for the DUNE program, with a measured collection efficiency of
 252 2% [15]. The upgraded X-ARAPUCAs will be deployed in the second beam run of ProtoDUNE-SP
 253 and later in DUNE FD1, however two prototypes were already inserted in ProtoDUNE-SP for the
 254 xenon doping run.

255 The two X-ARAPUCA (XA) detector units, called supercells, were installed on a dedicated
 256 support (see Figure 4). They are placed behind the APA-6, upstream with respect to the beam, at a
 257 distance of 22.7 cm from the frame (see Figure 5). The trigger for these detectors is not connected
 258 to the main ProtoDUNE DAQ. Instead, it is obtained from cosmic rays, through a standard triple
 259 coincidence of 15.5×44 cm plastic scintillators, located on the cryostat roof, 1.15 m far from the
 260 active volume. The three paddles select a solid angle of ~ 0.43 steradians, resulting in an average
 261 trigger rate of about 1 Hz.

262 The two supercells are identical but for the presence, on the top one, of a fused silica window,
 263 which is completely opaque to 128 nm radiation, whereas it has a measured transparency of $\sim 80\%$
 264 for 178 nm photons. For this reason, this detector collects only light from xenon de-excitation and

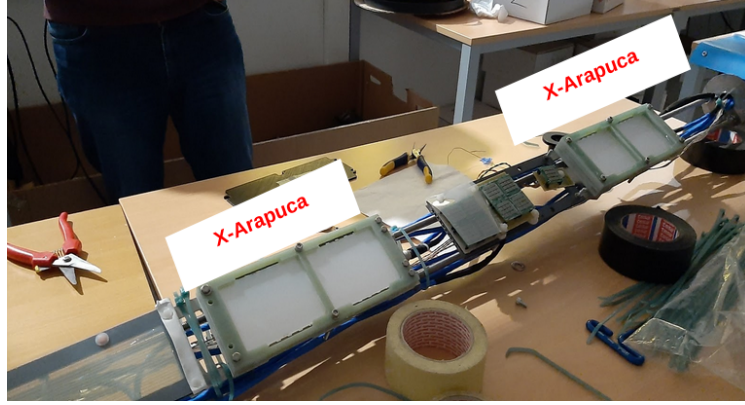


Figure 4: X-ARAPUCA detectors installed on a dedicated support (see 3D model in Fig. 5) and ready for insertion in the ProtoDUNE-SP cryostat.

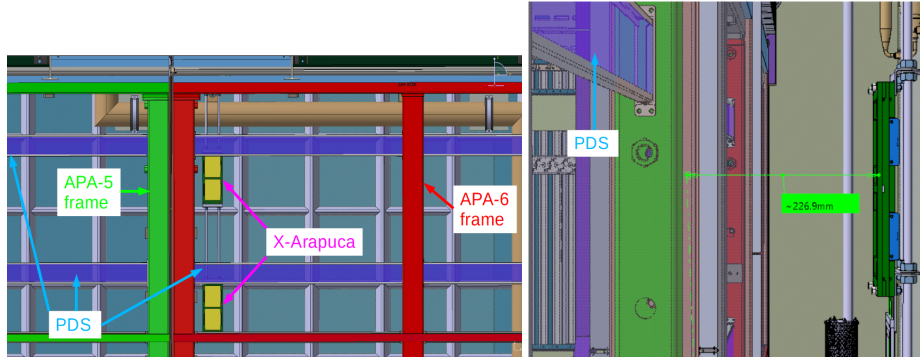


Figure 5: Top: front view of the two X-ARAPUCA detectors inside the ProtoDUNE-SP cryostat. In green, the frame of APA-5, in red the frame of APA-6, in blue the PDS bars. Bottom: side view, showing the position of the of the X-ARAPUCAs with respect to the APA frames and PDS.

265 will be labeled in the following as “Xe-XA”. The bottom supercell is instead sensitive to both argon
 266 and xenon light, and it will be referred to as “Ar+Xe-XA”.

267 The X-ARAPUCA light collection efficiency was measured in two prototypes, one $10 \times 8 \text{ cm}^2$ in
 268 size at Unicamp, Brazil [29] and the other $20 \times 7.5 \text{ cm}^2$ in size at INFN Milano-Bicocca, Italy [30]:
 269 the latter is of the same type and size of those deployed in this work. From these tests, an average
 270 effective Photon Detection Efficiency (PDE) of $\sim 2.3\%$ is obtained.

271 Both X-ARAPUCA are equipped with Hamamatsu MPPCs S13360-6050VE [31] with a $6 \times$
 272 6 mm^2 active area and 1.3 nF terminal capacitance. They were operated with a bias of 47.8 V ($+4.8 \text{ V}$
 273 OV). This value was chosen to guarantee the SiPMs PDE $> 50\%$ and to partially compensate for the
 274 lack of a cold front-end amplifier. Each supercell features two windows, both equipped with two
 275 arrays of four SiPMs positioned against the long sides of the WLS bar: the SiPMs within each array
 276 are readout in parallel, resulting in 4 readout channels per detector, and their signal is extracted via
 277 CAT6 cables. Readout is performed by a customized version of the standard SiPM Signal Processor
 278 (SSP) board in use for ProtoDUNE-SP run-1 [32].

279 **4 Cryogenics operations for xenon doping in ProtoDUNE-SP**

280 The ProtoDUNE-SP cryostat contains 770 tons of ultra pure LAr at 87.5 K, that is continuously
 281 purified through an ad-hoc cooling-recirculation plant. The Cryostat and the cryogenic plant are
 282 described in detail in [14].

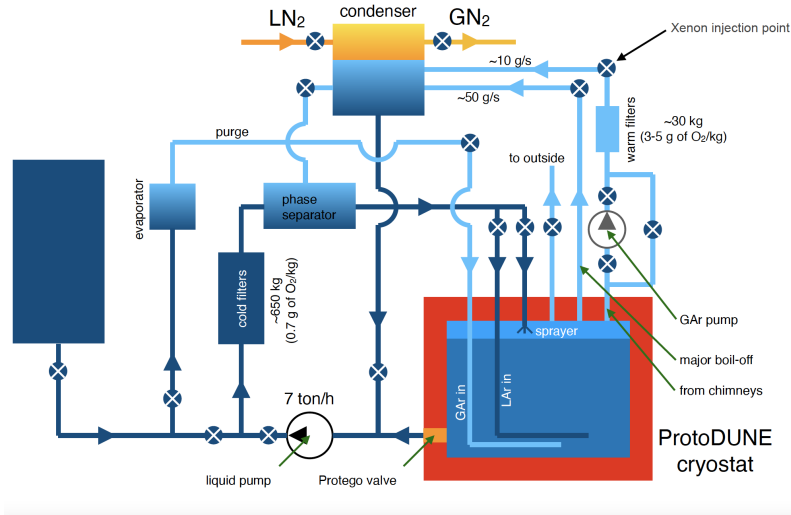


Figure 6: Schematics of ProtoDUNE-SP cryogenic system.

283 The system layout is depicted in Figure 6. It consists of two main circuits, for liquid and gas
 284 recirculation. The first circuit extracts LAr at the bottom of the cryostat by means of a cryogenic
 285 pump. The liquid is then forced through a cold purifier at a rate of ~ 7 ton/hour. The purifier consist
 286 of a first section filled with molecular sieve optimized to remove polar molecules, such as H_2O or
 287 CO_2 , and a second section containing copper deposited on alumina pellets, which adsorbs O_2 [33].
 288 The purified liquid is injected back at the bottom of the cryostat at a slightly warmer temperature
 289 (and lower density) to allow its upward diffusion, thus ensuring a better mixing with the bulk LAr
 290 in the cryostat.

291 The gas circuit is meant to both stabilize the operating pressure in the cryostat, by re-condensing
 292 the boil-off gas continuously produced by the residual heat input, and to purify the gas argon present
 293 in the ullage and in the feed-through chimneys. Indeed, these areas are expected to be heavily
 294 polluted, due to the degassing of materials (mainly the cables) present in this area.

295 Preliminary tests performed by the collaboration at CERN, with smaller LAr-TPC prototypes
 296 equipped with gas recirculation/purification systems, demonstrated that xenon can be efficiently
 297 mixed with LAr by injecting it in the gas phase, before the re-condensation. Several mixing ratios
 298 were tested, showing that the Ar/Xe ratio must be above 10^3 to avoid the solidification of the
 299 xenon on the walls of the condenser. This *freeze-out* effect is observed as, at the highest xenon
 300 concentrations, the pipes of the condenser get clogged up and the argon re-circulation stops. For
 301 this reason, xenon injection in ProtoDUNE-SP was performed through the gas argon recirculation
 302 system (see Section 4.2).

303 **4.1 Nitrogen contamination**

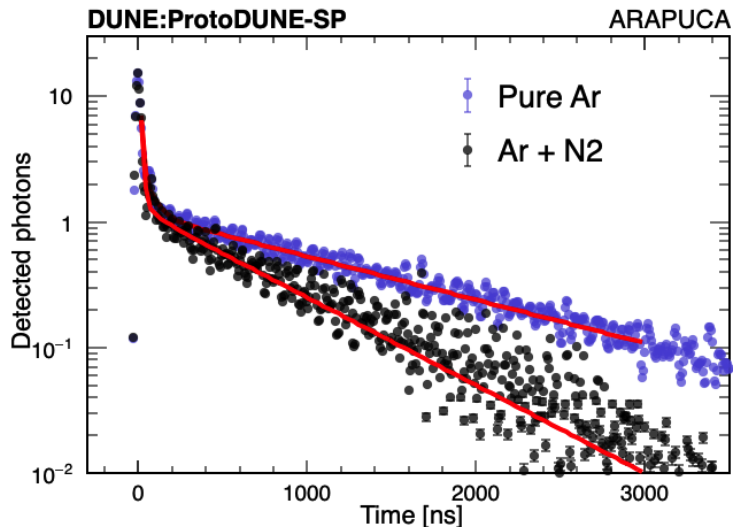


Figure 7: ProtoDUNE ARAPUCA module deconvoluted waveforms. Blue: “pure” Ar (before the air contamination), Black: after air contamination and purification (only N₂ contaminant is present). Pure argon waveform is scaled to have the same maximum amplitude on both waveforms.

304 As already mentioned, during the long cosmic run of ProtoDUNE-SP, a sudden failure in
 305 the warm gas re-circulation pump occurred, releasing a certain amount of air inside the detector.
 306 Molecules like O₂, CO₂ and H₂O were efficiently removed by the purification system, during the
 307 three weeks of recirculation through the filters, following the event. However, the system cannot
 308 remove N₂, which stayed in the detector until the end of the run. As mentioned in Section 2, nitrogen
 309 affects scintillation light emission, through the process of quenching. This effectively prevents the
 310 emission of scintillation photons from the slow component of the argon scintillation light.

311 As an example of the effect of N₂ quenching of LAr scintillation light, Figure 7 shows the typical
 312 profile of the scintillation light pulses for non-polluted LAr and LAr + N₂ after contamination, as
 313 obtained from ProtoDUNE SP data (specifically from the ARAPUCA module installed in APA 6).

314 By measuring the value of the decay-time constant of the argon triplet scintillation light
 315 component in both conditions [34], we can compute [23] the total amount of N₂ that is present in
 316 LAr: $\sim 5.4 \pm 0.1$ ppm, and derive the quantity leaked in during the accident: $\sim 5.2 \pm 0.1$ ppm. The
 317 initial (pre-accident) concentration estimated with this method is ~ 0.2 ppm N₂, compatible with
 318 the value provided by the LAr supplier (AirLiquide). This was regularly cross-checked with direct
 319 measurements performed during argon deliveries.

320 **4.2 Xenon doping campaign of ProtoDUNE SP**

321 The xenon doping run of ProtoDUNE-SP was started in February 2020 and lasted five months,
 322 with the goals of studying light emission in the presence of xenon, as well as long term stability
 323 and uniformity of the doped xenon inside the cryostat. It became even more important after the
 324 unexpected pollution event described above.

325 As mentioned, the xenon injection point is placed along the chimney boil-off re-circulation line
 326 (see Figure 6), after the gas purification filter but way before the condenser, to allow for full mixing
 327 within the gas flow. The maximum xenon mass flow rate was set to 36 g/h, to be well within the
 328 Ar/Xe ratio limit described above; this corresponds to 50 ppb/hour in the ProtoDUNE-SP detector.
 329 Based on the numerical (CFD) simulation of the LAr flow within the ProtoDUNE cryostat [35]
 330 [Asked to APB what to do with non-published references], the xenon injected at this rate is expected
 331 to be uniformly distributed in LAr within few hours. A detailed description of all steps of the doping
 332 procedure, and the lessons learned while performing it, is reported in Appendix A.

333 The run consisted in six injections, the last two of which were performed back-to-back over
 334 few days: for this reason, they are considered as one in the rest of the paper, from the point of view
 335 of the analysis. The amount of xenon injected in each step and the corresponding concentration
 336 inside the cryostat is summarized in Table 1. Combining all the doping steps, we injected 13.6 kg
 337 of xenon into the cryostat. This corresponds to 18.8 ppm of xenon concentration by mass in the
 338 0.77 kt LAr of ProtoDUNE-SP.

Table 1: Six xenon doping steps in ProtoDUNE-SP. The dates, doped xenon mass in grams and concentration in ppm by mass are given for each doping step.

Doping	Date	Doped Xe[gr]	Doped Xe[ppm]
1	13-14 February 2020	776	1.1
2	26-28 February 2020	2234	3.1
3	3-8 April 2020	5335	7.4
4	27-30 April 2020	3192	4.5
5	15-16 May 2020	400	0.6
6	18-20 May 2020	1584	2.2

339 Extensive data taking during each injection and between the dopings was performed, both with
 340 the ProtoDUNE photon detection system and with the dedicated X-ARAPUCA. The evolution of
 341 the scintillation light emission was monitored during the whole campaign, as a function of the
 342 amount of injected xenon.

343 5 Analysis of the X-ARAPUCA data

344 The X-ARAPUCA data are acquired with a standalone SSP that communicates with a local DAQ
 345 system that collects and saves data. When a cosmic ray triggers the three paddles within the
 346 coincidence window, the SSP starts digitizing the input signals coming from the SiPMs. The SSP
 347 implements a digitizer that samples at 150 MHz with a 14 bits resolution and an aggregator that
 348 streams out a 2000 samples waveform for each trigger ($\sim 13.3 \mu\text{s}$).

349 At the beginning of the run, an unexpected source of noise was found to be generated by the
 350 trigger electronics. In order to mitigate this noise, a subset of triggered events with no detectable
 351 physical signal was identified and their recorded pulses were averaged. We employed the averaged
 352 empty triggers to remove noise from the actual waveform.

353 A monitoring of sensors and electronics was carried on during all the acquisition period
 354 analyzing the Single PhotoElectron (SPE) response of the system. A peak finder algorithm searches

355 photoelectron pulses in the tail of each acquired signal, i.e. well beyond the triggered pulse. The
 356 integral of this sub-sample of data is then histogrammed. The resulting distribution exhibits a first
 357 peak that represents the pedestal (events with no photo-electrons) and following n^{th} peak represents
 358 respectively n photoelectrons. The first two peaks are fitted with two gaussians and the difference
 359 in the mean values is the SPE charge. Fig. 8 shows its stability along the entire run. The outcome
 360 of these quality tests demonstrated that the X-ARAPUCA system ran in stable conditions during
 361 the entire doping campaign.

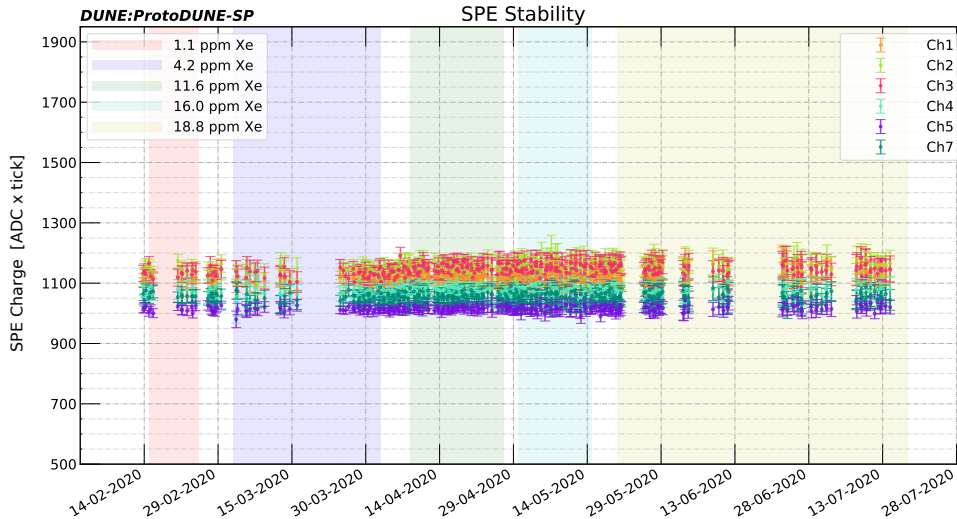


Figure 8: Mean SPE charge stability for all runs and each channel. Runs cover an overall six-month doping period, coloured areas represent specific dopings.

362 5.1 Data selection and deconvolution

363 The data acquired with the X-ARAPUCA detectors were first converted into a ROOT TTree and pre-
 364 processed applying a moving average filter to reduce the white noise and subtracting the baseline.
 365 For each waveform the integral, peak height in ADC counts and the peak time are computed and
 366 recorded.

367 The data are selected applying two main quality cuts, first the saturated events are discarded
 368 imposing a maximum on the peak-height parameter associated to each waveforms. The threshold
 369 value takes into consideration the electronics saturation level. Second we removed events with an
 370 ill-defined baseline or with a relevant pileup. These are events where a scintillation signal is present
 371 in the pretrigger region ($1 \div 200$ ticks) or in the ending of the signal ($1300 \div 2000$ ticks). The
 372 waveform are thus discarded if they cross a threshold of 10 photo-electrons in the respective defined
 373 regions.

374 The waveforms passing these cuts are averaged to reconstruct the response function of the
 375 detector. The information enclosed in these waveforms is the convolution of three main effects

376 $S(t) = L(t) \otimes XA(t) \otimes h(t)$: the scintillation light time-profile $L(t)$, the X-ARAPUCA $XA(t)$
377 time-response and the electronics $h(t)$ response. The first is characterized by the light yield, the
378 emission properties of the mixture (Ar+Xe+N₂) and by the light propagation including absorption
379 and Rayleigh scattering. The second is characterized by the X-ARAPUCA response, in particular
380 by the absorption and re-emission of the wavelengthshiffters. As the re-emission delay of TPB and
381 PTP is considered below < 10 ns [CITATION], we can consider the time dependence of this effect
382 negligible. The third effect $h(t)$ is due to the response of both sensors and the electronics to a single
383 photon signal. To retrieve the scintillation signal $L(t)$ containing the relevant physical information,
384 this last effect needs to be deconvolved as the most relevant. In fact, the signal coming from SiPMs
385 is proportional to the number of photons but has a time-extension of about 400 ns, comparable with
386 scintillation signals.

387 To deconvolve this effect, a (time-dependent) template for the single photo-electron is needed.
388 A filter for peak finding is implemented to search single photo-electrons in the pre-trigger region.
389 Once selected, they are aligned at the same time and averaged; the resulting shape is then fitted.
390 The fit function consists of a double exponential convoluted with a Gaussian to account for white
391 noise: $h(t) = Gaus(t; \mu, \sigma) \otimes (\exp[-t/\tau_1] - \exp[-t/\tau_2])$. The two time constants represents
392 respectively the SiPM avalanche discharge ($\tau_1 \sim 400$ ns) and the electronics shaping time.

393 More than one deconvolution technique was applied independently on the waveforms, to cross-
394 check the results. One such technique is based on the Gold algorithm [36] and the parameters were
395 optimized to minimize the reconstructed fast component of LAr, as well as the noise. Another
396 technique makes use of a custom FIR filter to simultaneously de-noise the waveforms and filter out
397 the shape of the single photo-electron response function. The filter employed is analogous to the
398 one presented in [37], although it lacks the zero-area requirement. It is a finite-length cusp-like filter
399 with a 33 ns flat top and the cusp shape parameter $\tau_s=33$ ns. It is tailored for each of the 6 channels
400 to properly take into account the individual exponential decay of channel response function.

401 5.2 Effects of xenon on LAr light

402 The effect of the energy transfer, as introduced in Section 2, is clearly exemplified in Figure 9. The
403 plots show examples of waveforms that were deconvolved according to the technique introduced
404 in the previous paragraph. The two panels refer to the two X-ARAPUCA detectors, showing
405 superimposed waveforms at different concentrations of doping. The overall shortening of the pulse
406 profile as a function of xenon concentration is evident in both cases. These data are collected with
407 the presence of nitrogen, therefore the long tail of the typical argon signal is expected to be strongly
408 reduced with respect to the non-polluted argon case (cfr. 7. In particular in the bottom panel of
409 the figure, referring to the Xe-XA device, it is then possible to appreciate the concurrent effect of
410 xenon: the increase in total light (the larger area under the pulse) is due to dimer excitation being
411 transferred from argon to xenon.

412 After the SPE calibration, the absolute number of photons detected by the two X-ARAPUCA
413 detectors can be extracted during the entire doping run. Fig. 10 shows that this number increases
414 during each injection and it remains stable during the monitoring periods, for both X-ARAPUCA.
415 This general increasing trend testifies to the effectiveness of energy transfer, especially in the
416 presence of N₂. Indeed, the light that was lost after the pollution event appears to be recovered once
417 xenon starts competing with N₂-induced quenching. We note that, while it is widely reported in

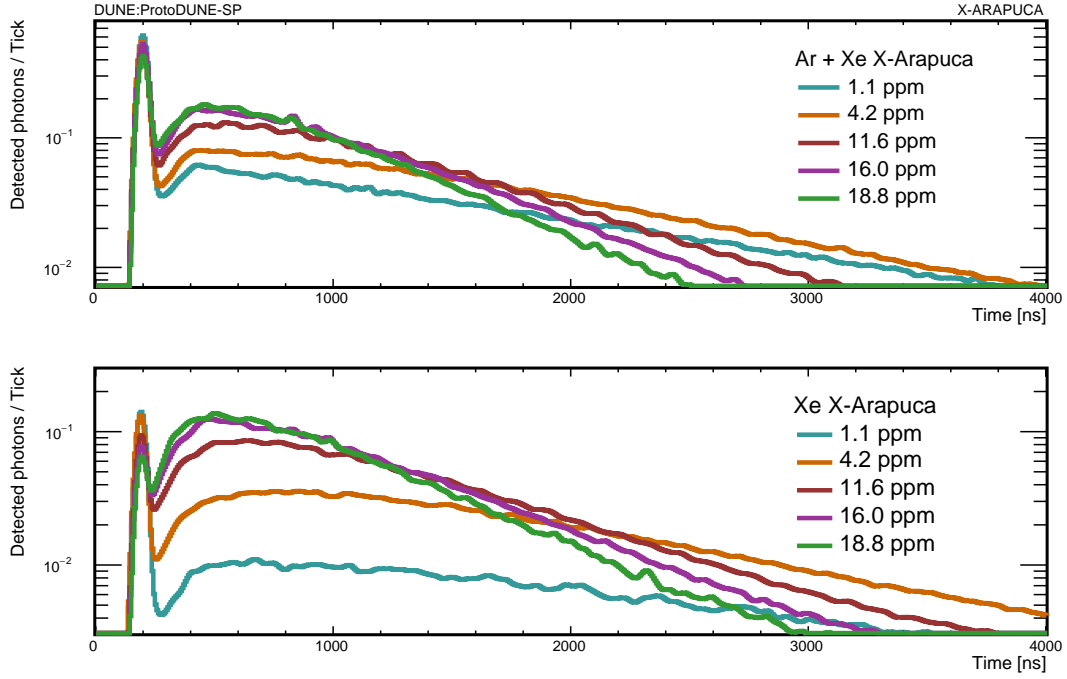


Figure 9: SPE-deconvolved average waveforms at different stages of xenon doping (after nitrogen pollution). Top panel: *Ar+Xe-XA*; bottom panel: *Xe-XA*. Only events with at least three detected photons in the *Ar+Xe X-ARAPUCA* module are selected.

418 literature citation that xenon effects on light emission extend up to few hundreds ppm concentration,
 419 in these conditions and with these detectors, the increase appears to flatten out at the level of around
 420 16 ppm of xenon, indicating a possible saturation effect. It worth noting though that further data
 421 collected in the following two months are compatible with a flat trend, which hints to a stability in
 422 time of the xenon doping effect.

423 In this picture it is possible to appreciate the effect of the presence of the TPC electric field
 424 on light production, as well. Since the absolute amount of light produced is considered here,
 425 drops in the number of photons is expected when the electric field is on. Indeed, its presence
 426 drifts away electrons that would otherwise recombine with their parent ions, thus reducing the
 427 overall light output of the detector. The mentioned dips are clearly visible on the data-sets of both
 428 *X-ARAPUCA*.

429

The actual amount of liquid argon scintillation light (128 nm) that is shifted to xenon light (178 nm) is the observable chosen to evaluate in a more quantitative way the efficiency of the energy transfer between argon and xenon excimers. This is defined as the ratio between the xenon light and the total light detected for each run, that is, in this case, the ratio of the average light seen by the *Xe X-ARAPUCA* (only sensitive to xenon, see Sec. 3.3) to the average light seen by the *Ar+Xe X-ARAPUCA* (sensitive to the total light).

$$\text{Fraction} = \frac{\text{Xe light}}{\text{Ar light} + \text{Xe light}} \equiv \frac{\langle \gamma_{\text{Xe XA}} \rangle}{\langle \gamma_{\text{Ar+Xe XA}} \rangle} \quad (5.1)$$

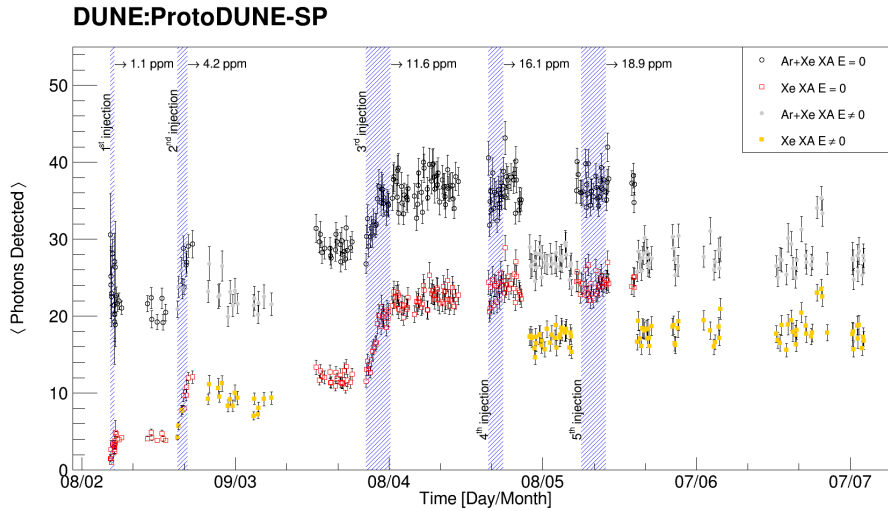


Figure 10: Light collected by the two X-ARAPUCA modules, in units of detected photons. The amount of collected light increases at each doping. Sudden drops are caused by the activation of the HV system of ProtoDUNE-SP and, hence, the presence of the electric field. Shaded areas show the time when xenon was injected.

430 Figure 11 shows the above ratio as a function of time, increasing at each doping. Also in this
 431 case, the trend tends to flatten out at around 16.1 ppm, reaching a stable value of 0.65. In this
 432 configuration, one can assume that the triplet component of the argon light is completely drained
 433 by the presence of xenon. The ratio remains stable outside the injection periods (dashed regions).

434 It is worth noting that in this case, since only relative amounts of light are considered, the
 435 trends of the two data-sets with and without the TPC electric field are superimposed. This suggests
 436 no detectable interference between the electric field presence and the argon-xenon energy transfer
 437 process, at least at the level of this local measurement. Some differences appear to arise only when
 438 considering the profile of collected light as a function of the distance of the track from the light
 439 sensors (see Section 6).

440

441 Further information about the effect of xenon presence can be extracted by surveying the
 442 evolution of the amount of so-called “fast” and “slow” light components independently, as a
 443 function of time.

444 Figure 12 shows what is here defined as “slow light”, i.e. the superposition of the residual
 445 triplet argon scintillation light and part of the xenon-converted light. This is defined from the
 446 integral of the waveform in a fixed time-window, starting 11 time-ticks (~ 74 ns) after the trigger
 447 until the end of the recorded pulse. The start-time value for the separation between the fast and slow
 448 components accounts for the rise-time of the pulse, plus around 3 times the decay-time constant
 449 of the argon singlet light. As reported in literature (e.g. [22, 23]), this should be around 6-7 ns,
 450 however the convolution with the time response of ProtoDUNE SP light detectors [15] results in a
 451 fitted singlet decay-time constant of around 13-14 ns: hence the chosen value to separate the fast
 452 and slow light components in this particular set-up.

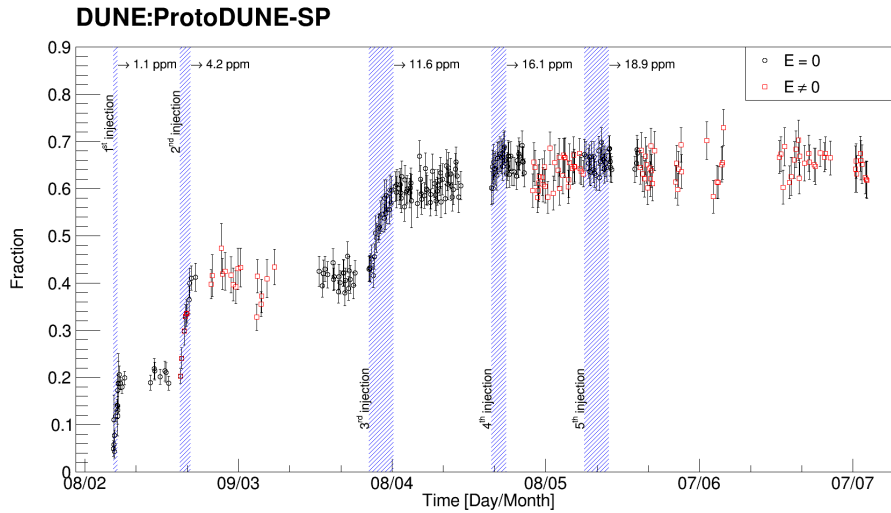


Figure 11: Fraction of the argon light (128 nm) that is converted to xenon light (178 nm): $\frac{Xe}{Ar+Xe}$. The ratio increases with the doping and reaches a plateau around 0.65 for xenon concentration greater than 16.1 ppm. The red points correspond to data collected with the nominal TPC electric field, while black points refer to data with no electric field. Shaded areas indicate xenon injections.

453 The number of photons from the slow component is shown to increase with xenon concentration,
 454 with a trend quite similar to that of the overall light output produced in Figure 10. This is expected
 455 and consistent with the fact that the energy transfer process involves the argon long-lived triplet
 456 state (see Section 2. As a further evidence of the origin of this light increase, the trends observed
 457 for the two X-ARAPUCA are almost identical, i.e. it can be traced back entirely to 178 nm xenon
 458 scintillation light.

459 Figure 13 shows the evolution of the “fast” light component with time. This is defined as the
 460 fraction of the integral of the waveform taken between the trigger time and 11 time-ticks after that.
 461 The plot shows a very quick drop of this light component during the first doping period, followed
 462 by a minimal though pretty stable output throughout the rest of the run.

463 The quick drop of the fast light that is observed at the beginning of the doping comes as
 464 unexpected. Indeed, it cannot be explained *a priori* by the xenon energy transfer process, as the
 465 argon singlet decay time ($\tau_s = 6$ ns) is much shorter than the time required for the $Ar_2^* - Xe$ interaction
 466 to take place. However, there are studies in literature ([38]) that report an actual absorption of the
 467 argon light by xenon: according to these results, the absorption profile of xenon partially overlaps
 468 with the 128 nm scintillation peak of argon, which has a FWHM of around 10 nm. The absorption
 469 process seems to be saturating already at the lowest concentrations of xenon, which is consistent
 470 with what is observed in our data.

471 If that is the case, the residual fast component detected in the fully sensitive X-ARAPUCA
 472 can be ascribed to the singlet argon excimers surviving absorption. Going back to Figure 9, one
 473 can notice that such draining effect of the fast component is indeed far more clearly visible in the
 474 xenon-only sensitive X-ARAPUCA (bottom panel).

475 Nonetheless, figures 9 and 13 show that despite the process described above, on average

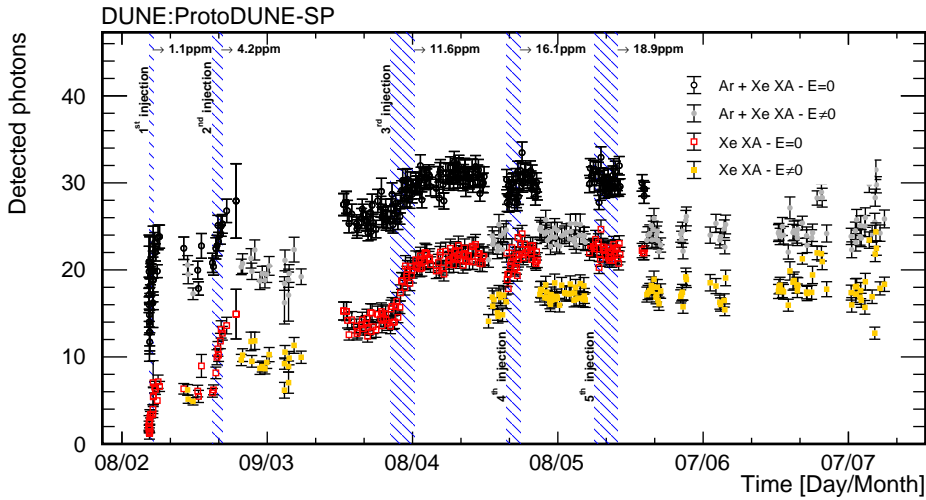


Figure 12: Time survey of the mean number of photons in the slow light component detected by the $Ar+Xe-XA$ and by the $Xe-XA$, for runs with ($E \neq 0$) and without ($E = 0$) electric field. Shaded areas indicate xenon injections. Only events with at least three detected photons in the $Ar+Xe$ X-ARAPUCA module are selected.

476 one/two *fast* photons (i.e. within ~ 74 ns from trigger) are still detected by the xenon-only sensitive
 477 X-ARAPUCA, for xenon concentration ≥ 1.1 ppm. Their origin is not obvious, however possible
 478 sources have to be spurious, if one stands by the xenon-absorption hypothesis: Cherenkov emission
 479 from cosmic rays secondary particles crossing the device entrance window; wavelength-shifted
 480 light escaping other PDS modules and entering the not light-tight device inner volume; spurious
 481 events inside the latter.

482 The analysis of the X-ARAPUCA data implies a local measurement of the xenon effect on
 483 argon scintillation light, made on a specific set of data: vertical and almost vertical cosmic muons.
 484 As a whole, the analysis yields a general confirmation of the assumed model of argon-xenon
 485 energy transfer, as known from literature. It also confirms the successful implementation of the
 486 doping in ProtoDUNE-SP and hints at a reasonable stability in time: the effect of xenon increases
 487 during injections and appears not to degrade soon after the doping is completed. These data do
 488 however leave some open questions, especially concerning the fast light component detected by
 489 the X-ARAPUCAs. In order to better understand this aspect, further data would be fundamental.
 490 Soon after the ProtoDUNE SP xenon run, a similar campaign was carried out with the other DUNE
 491 prototype present at CERN, ProtoDUNE Dual Phase (DP). Analysis of those data is in progress
 492 by the involved people and the next step will be to combine the two data sets for a joint analysis,
 493 that should shed more light on the physics process and help better understanding the results of both
 494 detectors.

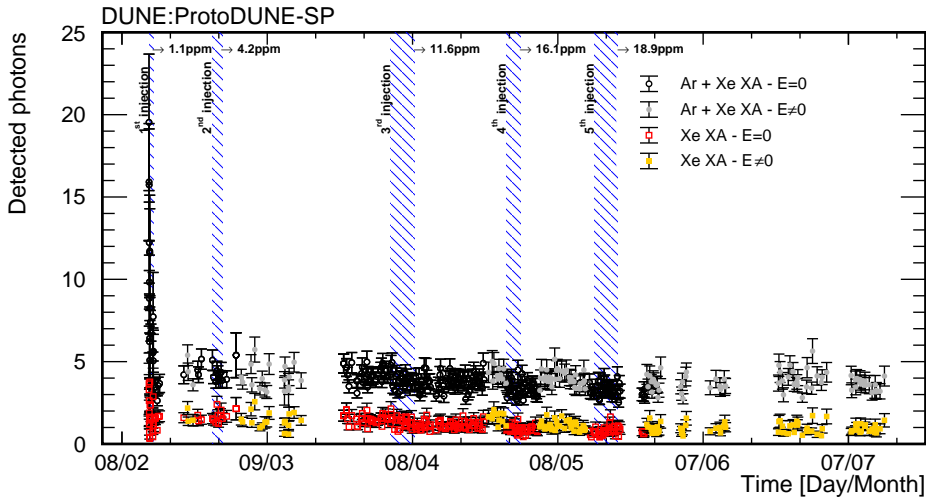


Figure 13: Time survey of the mean number of photons in the fast light component detected by the $Ar+Xe-XA$ and by the $Xe-XA$, for runs with ($E \neq 0$) and without ($E = 0$) electric field. Shaded areas indicate xenon injections. Only events with at least three detected photons in the $Ar+Xe$ X-ARAPUCA module are selected.

495 6 Analysis of the ProtoDUNE-SP PDS

496 The Photon Detection System of ProtoDUNE-SP provides an independent handle to observe the
 497 changes in the scintillation medium as a consequence of doping or contamination. It also has
 498 the added benefit of allowing direct injection comparison with the original run period before nitrogen
 499 contamination [15]. To this end, the data-set discussed in this Section is divided into multiple epochs:
 500 a period before xenon doping and nitrogen contamination, described as the first ProtoDUNE-SP run;
 501 a period after the first run, with only nitrogen present in the drift volume; and a xenon doping period,
 502 where xenon was injected over a period of few months. All periods feature different configurations
 503 of the TPC electric field, which varies from zero to the nominal setting (500 V/cm) significantly
 504 changing the total absolute amount of light available. All of the following ProtoDUNE PDS studies
 505 use light collected from through-going cosmic-ray muons selected in coincidence with the CRT.

506 6.1 Triggering, data selection, and collected light

507 Triggering in ProtoDUNE-SP relies on the central DAQ and typically involves a coordination
 508 between two or more subsystems. For the ProtoDUNE-SP PDS, two major triggering schemes
 509 exist which both depend on a coincidence between the upstream and downstream modules of the
 510 Cosmic-Ray Tagger (CRT). The trigger coincidence window length, pre-scaling, and trigger mask
 511 have varied throughout the run configurations as indicated by the red lines in each of the Figures
 512 from 14 to 17. If the TPC is available and at the proper potential, a CRT coincidence is coordinated
 513 with through-going tracks, allowing a comparison of the orientation of the track, reconstructed by
 514 the TPC, to the vector which intersects the center of both triggered CRT modules strips. A quality
 515 cut is made on single tracks that meet the TPC reconstruction and selection criteria, have a viable
 516 trigger, and pass a quality cut of $\cos \theta > .999$, indicating a deviation of less than a degree between

517 track from TPC and trigger from CRT. If the TPC is not available, a selection is made based on
518 matching distinct PDS coincidences across APAs requiring at least two photon detectors in two
519 different APAs within a time coincidence of $13 \mu\text{s}$.

520 The light collected from the selected sample is summed across a single detector and assigned
521 a *radial distance*, which is defined as the straight line distance from the photon detector to the
522 track when they are in the same XY-plane. A Gaussian or Poissonian fit to the collected light at
523 each cm of radial distance is performed to obtain the most probable value, which represents the
524 expected amount of light observed from a passing muon at a given radial distance where the choice
525 of distribution depends on the bin statistics. An analysis of the average collected light as a function
526 of time and with different trigger periods is shown for different regions of the detector and distinct
527 SiPMs in Figures 14 to 17. Despite the variations in triggers, the average amount of light collected
528 does not change appreciably with trigger variation. All figures draw a consistent picture across the
529 detector volume, SiPM models and detection technologies, when compared with the X-ARAPUCA
530 results produced in the previous Section. The average amount of light detected in ProtoDUNE
531 drops after the nitrogen contamination and then it increases again in steps, with each new doping
532 with xenon. Data collected with and without the TPC electric field consistently show two parallel
533 trends of increase, due to the different available total amount of scintillation light. The data from
534 runs with the TPC electric field on show larger spread, as anticipated, due to a wide number of
535 trigger configurations used for these runs. There is particularly large spread across all runs taken
536 during June 15-27 of 2020, denoted in Figures 14 to 17 with at large concentration of red lines.
537 The runs were taken with a large variety of CRT Trigger masks to collect a wide range of tracks at
538 varying radial distances to collect enough data for Figure 18 over the short time allocation we had
539 for these runs. Each CRT mask was designed to select a small subset of the total radial distance
540 range, and this masking effect paired with short run times leads to a high volatility in average light
541 yield for the individual runs. After June 27, 2020, indicated by the final red line in these plots,
542 the CRT masking was reset to match that of previous runs, and a consistent average light yield is
543 again observed. It can also be noted that the average light yield at the end of the Xenon doping
544 campaign is in the range of the average light yield before the nitrogen contamination, showing that
545 the injection of Xenon works to counteract the effects of contamination. Figure 18 shows that this
546 recovery of light is not uniform with distance, but increases as the light source is farther from the
547 detector which agrees with expectations.

548 **6.2 Light recovery due to xenon injection**

549 As described in the previous Section, the amount of collected light by the ProtoDUNE PDS and
550 the changes in the characteristic light-pulse profiles (waveforms) can supply critical information
551 about how the injected xenon significantly alters the character of the scintillation light produced in
552 the detector. Furthermore, the use of the ProtoDUNE-SP PDS also allows constructing attenuation
553 curves that track the amount of detected photons as a function of the previously defined *radial*
554 *distance* between the tracks and the photon detectors. The following plots refer mainly to data
555 collected by the non-beam side ARAPUCA, i.e. those in the Left TPC, or *Beam-Left*, BL, with
556 respect to the beam direction (see Section 1). The phrase *Pure LAr* in the plots legends is short for
557 the data relative to the period before the nitrogen contamination. Fig. 18 clearly indicates that the
558 amount of light collected by the non-beam side ARAPUCA drops after the nitrogen contamination,

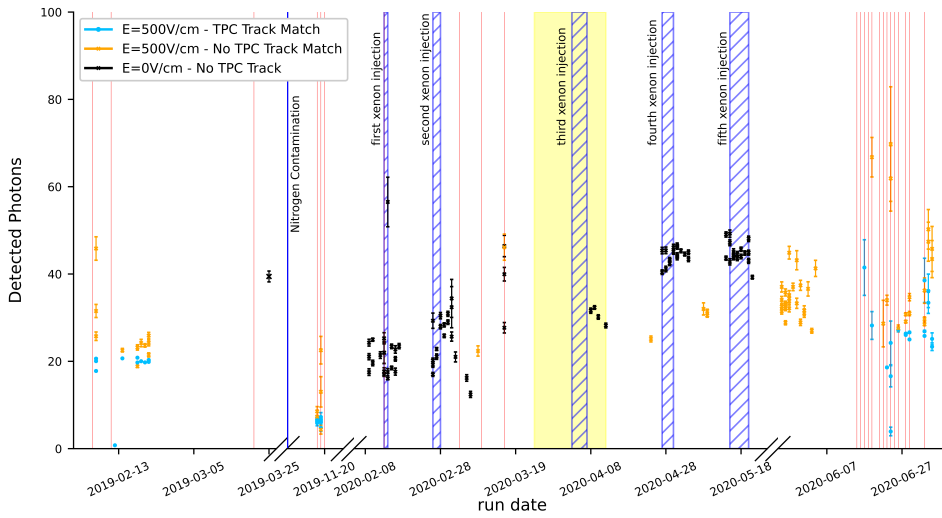


Figure 14: The figure shows the average number of photons detected in the ARAPUCA on beam left in the PDS over the entire nitrogen contamination and xenon doping period. Red lines indicate changes in the trigger configurations; blue lines indicate changes in the scintillation medium through nitrogen contamination or xenon injection, the yellow band indicates a period of operation where only APA 3 and APA 6 were operational.

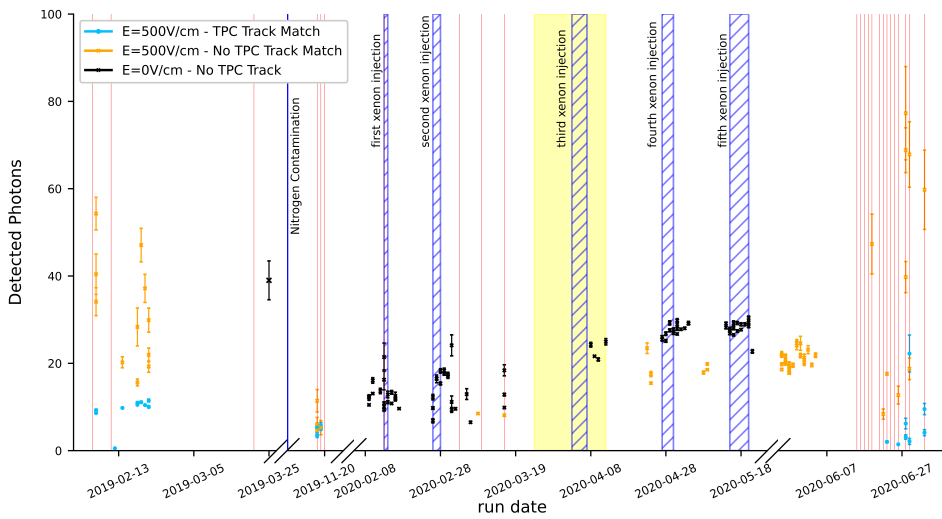


Figure 15: The figure shows the average number of photons detected in the ARAPUCA on beam right in the PDS over the entire nitrogen contamination and xenon doping period. Red lines indicate changes in the trigger configurations; blue lines indicate changes in the scintillation medium through nitrogen contamination or xenon injection, the yellow band indicates a period of operation where only APA 3 and APA 6 were operational.

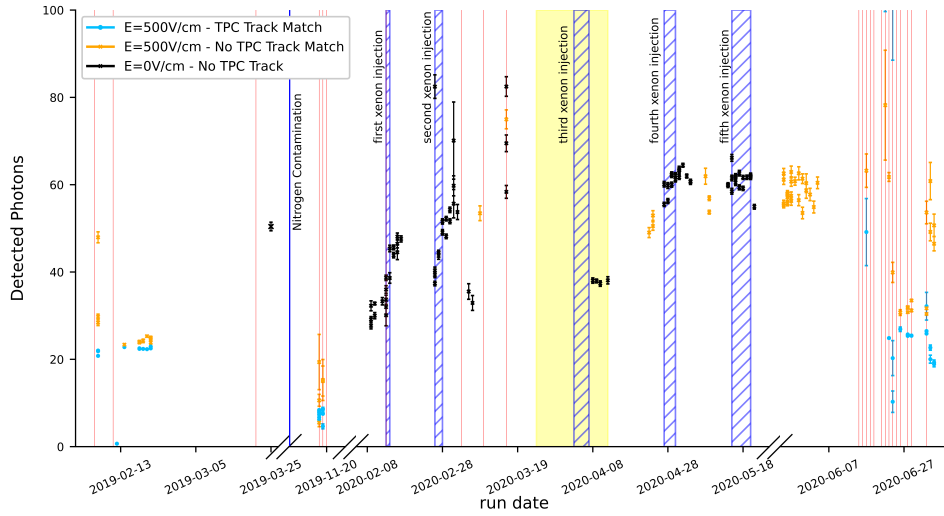


Figure 16: The figure shows the average number of photons detected in the Double shifted light guides with Hamamatsu MPPC sensors throughout the entire PDS over the entire nitrogen contamination and xenon doping period. Red lines indicate changes in the trigger configurations; blue lines indicate changes in the scintillation medium through nitrogen contamination or xenon injection, the yellow band indicates a period of operation where only APA 3 and APA 6 were operational.

559 but then increases again significantly after the xenon injection. The plots of the right column also
 560 highlight that the light recovery, quantified by the ratio of the light after doping over the amount of
 561 light before nitrogen contamination, increases with the distance from the photon detectors. Once
 562 again, comparing plots (a) to (d) with plots (e,f) the described behaviour is completely independent
 563 of the presence of the TPC electric drift field. This result is confirmed and enforced when comparing
 564 it with the same plots coming from data collected with other photon detection technologies: as an
 565 example, Figure 19 reports the same attenuation curves and ratios of light collected, with respect
 566 to the period before nitrogen contamination, for the non-beam side double shifted light guides,
 567 equipped with both SensL and Hamamatsu SiPMs. Figures 18 (b,f) and 19 (bottom panels) confirm
 568 that, due to the larger Rayleigh scattering length in LAr at 178 nm, with respect to that at 128 nm,
 569 the uniformity of response as a function of the distance from the detection plane increases after the
 570 doping. This mitigates the intrinsic non-uniformity of the DUNE PDS, which is installed only in
 571 the proximity of the TPC anode, i.e. inside the APAs.

572 The details of the overall light increase with respect to the nitrogen contamination period are
 573 shown in the comparison of the characteristic light waveforms across the doping period: Figure 20.
 574 Events used in these plots are a subgroup of all events showed in Fig. 18 (c) and (d). Selection was
 575 made using tracks with a defined geometry. The selected events mean radial distance is ~ 250 cm,
 576 with standard deviation of ~ 30 cm. The selection is needed as, given the differences between the
 577 argon and xenon light propagation, the waveform shape and integrals are expected to change with
 578 the distance of the event from the detector; see Figure 18.

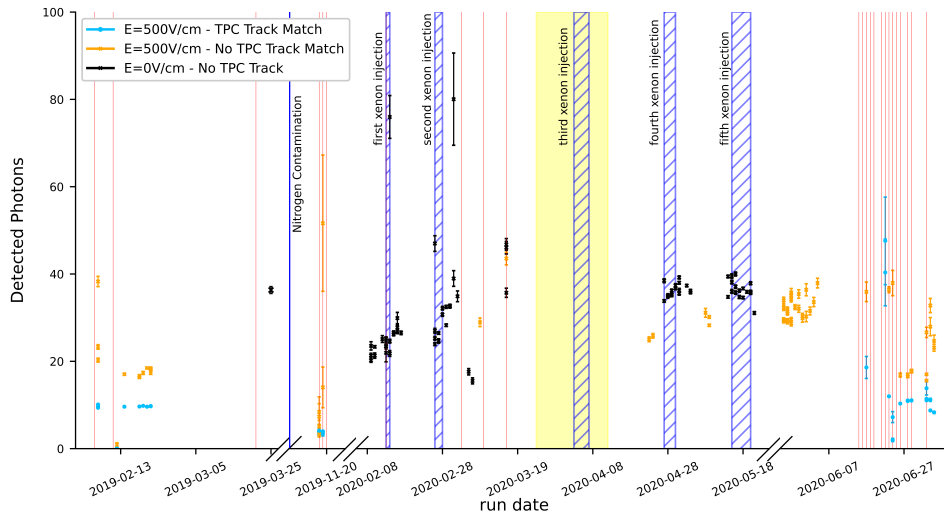


Figure 17: The figure shows the average number of photons detected in the Double shifted light guides with SensL SiPM sensors throughout the entire PDS over the entire nitrogen contamination and xenon doping period. Red lines indicate changes in the trigger configurations; blue lines indicate changes in the scintillation medium through nitrogen contamination or xenon injection, the yellow band indicates a period of operation where only APA 3 and APA 6 were operational.

579 Comments by Flavio: not explained where factor 5 below and 95% values come from; no
580 discussion on how this compares with expectation and present models/measurements. BR: response,
581 values come directly dividing average light from before and after doping and before and after
582 contamination. I don't know if we have expectation because we haven't done doping with so much
583 nitrogen contamination. This is a 'new' mixture and I'm not sure we understand microphysics
584 of absorption and energy transfer between molecules. Panels (a,b) demonstrate that, as the
585 concentration of xenon increases, the slow² component of the characteristic argon waveform is
586 increased by at least a factor of five. On the other hand, the characteristic argon fast component
587 is significantly reduced right after the first doping, but then it remains very stable throughout the
588 following doping steps. These trends are consistent with what is obtained from the analysis of the
589 X-ARAPUCA data, but on a global detector scale and with a different sample of tracks. Panels
590 (c,d,e) in Figure 20 summarise the changes in the average number of detected photons across the
591 full xenon doping period for the slow and fast components of the scintillation light, as well as for
592 the total collected light.

593 Comment by Flavio on fig 18 and related text. three results in these plots, to be better discussed
594 / separated: attenuation with and without Xe; light loss due to nitrogen (not shown for x-arapuca,
595 so 'new'); effect of rayleigh, with higher coll. eff. at large distance / lower at short distance.

596 To reinforce the statement made at the end of the previous subsection, the presented analysis
597 confirms on a global, detector-wide level, the results obtained on a local level with the dedicated

²For the analysis of the PDS data, the same definitions of *slow* and *fast* component of the scintillation light, in terms of interval of integration and given in Section 5, still hold.

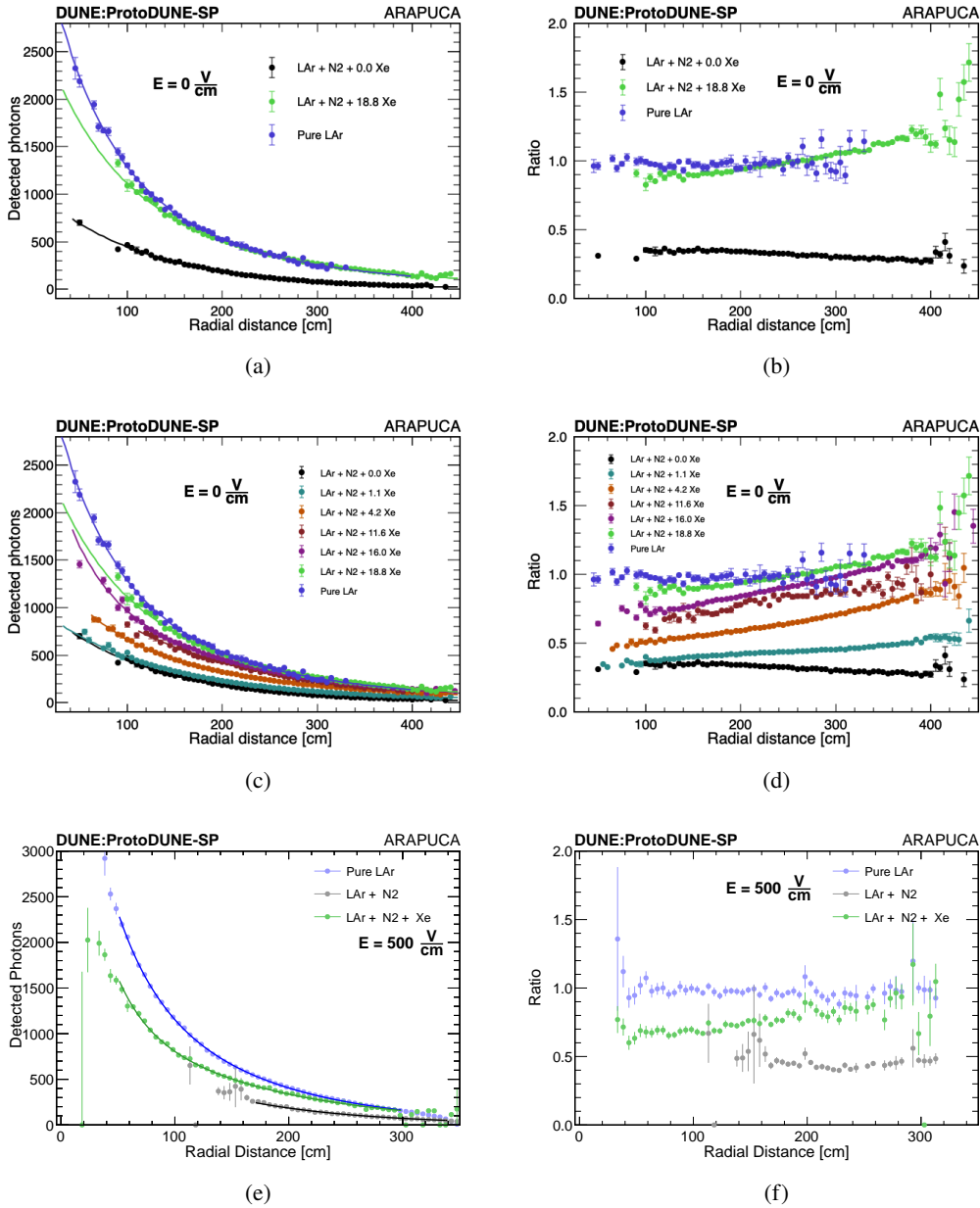


Figure 18: Light recovery demonstrated through attenuation curves after xenon injection with the non-beam side PDS ARAPUCA. The left column of plots shows the collected light versus radial distance, while the right column shows the ratio of collected light relative to the pure LAr and nitrogen-contamination periods. The top and bottom rows of plots show the measurement made without and with TPC electric field, respectively. The middle plots detail the gradual increase of collected light with increasing xenon concentration, with no drift field.

598 X-ARAPUCA detectors in Section 5. The comparison of results from different areas of the main
 599 active volume and the studies of the collected light profile as a function of distance from the photon
 600 detectors hint strongly at a successful doping procedure, which led to uniformly distributing xenon

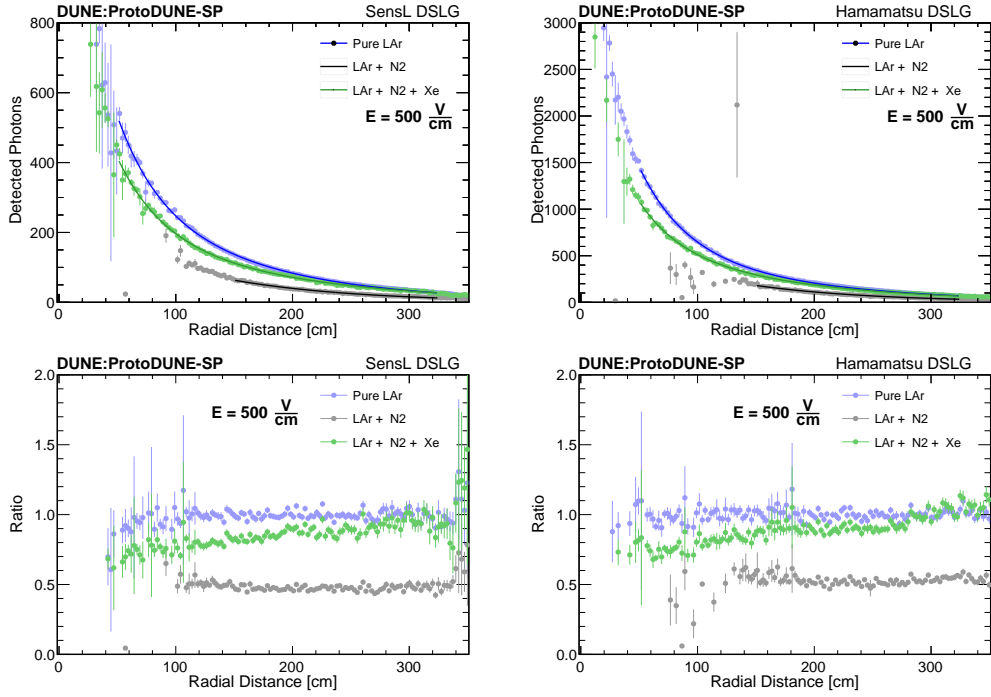


Figure 19: Light recovery as demonstrated through attenuation curves for the non-beam side double shifted light guides, divided by sensor technology, with the TPC drift field on. The top plots represent the collected light versus radial distance, whereas the bottom plots represent the ratio of collected light relative to the pure LAr and nitrogen-contamination periods.

601 across the detector volume. Such an encouraging result represents the necessary stepping stone
 602 towards the implementation of xenon doping at the much larger scale of the DUNE far detectors.

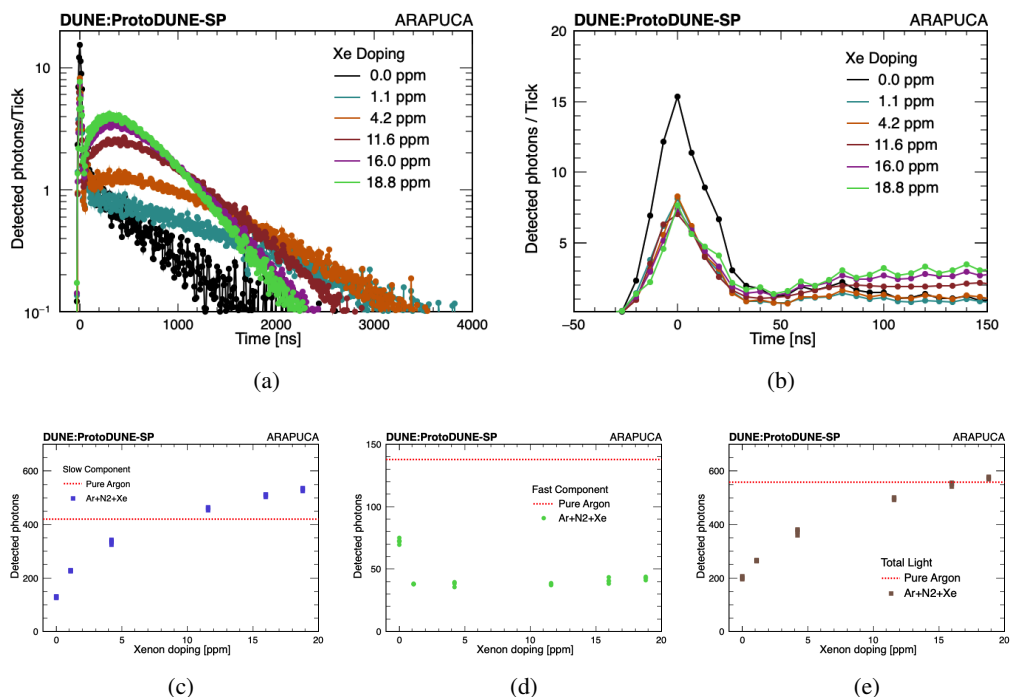


Figure 20: Top row: non-Beam Side ARAPUCA deconvoluted waveforms, changing in shape with the concentration of xenon. Bottom row: evolution of the fast, slow light component and total light as a function of xenon concentration, in the nitrogen contaminated scintillation medium (details of track selection for these plots is reported in text).

603 7 Charge reconstruction in liquid argon doped with xenon

604 During the xenon doping run, the operation of the ProtoDUNE SP TPC was monitored in order to
 605 understand whether the presence of the dopant would affect the charge collection.

606 A useful monitor of the stability of the ProtoDUNE TPC performance is the so-called *TPC*
 607 *signal strength*. In ProtoDUNE-SP, the primary contribution to charge deposits in the LAr is
 608 ionization from cosmic rays. The amount of collected charge is evaluated for each collection wire
 609 by summing all the calibrated charge deposits, over those regions where the signal is significantly
 610 above the noise level for the channel. The fraction of the originally produced ionization charge
 611 actually reaching each collection wire depends on the purity of the LAr, on the voltages applied to
 612 the wires and cathode planes, as well as on space charge effects [15]. The calibrated response of
 613 the detector relies on the electronics modules gain, which was evaluated with test-charge injections
 614 and was stable over the course of the run [39].

615 Figure 21 shows the TPC signal strength before, during and after the xenon filling, for those
 616 periods where APA data were collected with voltages at or near nominal values. Each point is
 617 evaluated by averaging the calibrated charge over all good collection wires in an APA for few
 618 thousand randomly triggered events, with acquisition windows of 3 ms in each event. The figure
 619 includes a line at 93 ke/channel/ms, typical reference for nominal voltages and high purity. The
 620 drop in signal strength on all APAs are due to episodes where the purity dropped.

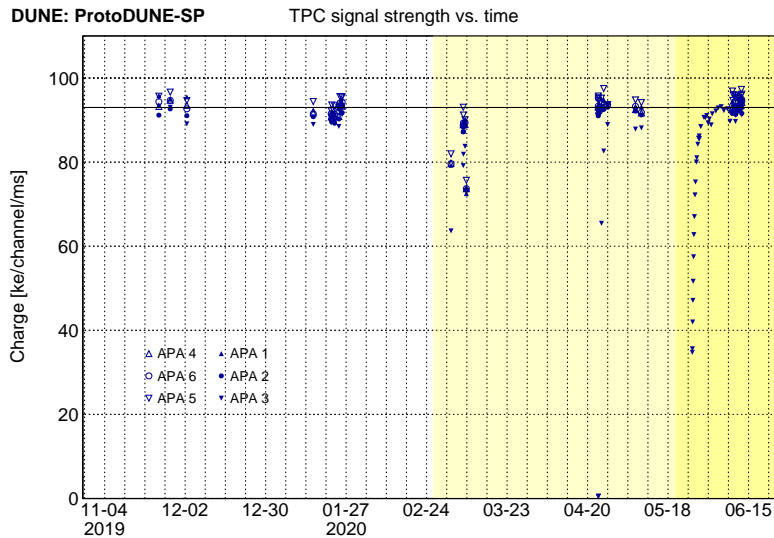


Figure 21: Signal strength versus time, near the time when xenon was injected. The doping period is highlighted in light yellow, whereas darker yellow represents xenon at maximum concentration. The drop at the beginning of the light yellow area corresponds to a drop in purity following the first injection (see Appendix A). Data points for APA 3 are consistently lower than other APAs after turning on the electric field, and steadily recover in the first few days, due to a problem on its grid plane biasing.

621 The xenon doping period is highlighted in light yellow, whereas the darker yellow refers
 622 to maximal xenon concentration. One can see that the average TPC signal strength in standard
 623 conditions remains at its nominal value before, during and after the xenon doping. This indicates
 624 that xenon has no observable effect on the fraction of charge reaching the collection wires, and
 625 therefore that it can be safely used in the DUNE far detectors.

626 8 Conclusions - NOT CORRECTED YET

627 In this paper we describe the first very-large-scale attempt at doping a liquid argon TPC with xenon,
 628 performed on ProtoDUNE Single Phase detector at CERN. Xenon doping of liquid argon is a known
 629 technique to enhance scintillation output of the medium and to ease light collection by shifting the
 630 photons to a higher wavelength. This can bring advantages to the physics program of the DUNE
 631 experiment, and it has been considered for its second far detector module, therefore a large scale
 632 test was in order.

633 In this paper we review the basics of the xenon-argon interaction and we describe the mixing
 634 procedure put in place for ProtoDUNE SP. The success of the doping on such a large scale (~ 1 kton
 635 LAr) was never tested, therefore we then performed a data taking campaign with the aim of studying
 636 the scintillation light output during and after the doping. This was done at the local level, with two
 637 dedicated X-ARAPUCA detectors expressly installed outside the TCP active volume, and globally,
 638 with the ProtoDUNE PDS.

639 Before the test, ProtoDUNE SP had suffered an accidental leak resulting in nitrogen con-
640 tamination at the few ppm level, that would significantly reduce the amount of light reaching the
641 photosensors. The presence of xenon increased the amount of collected light, both locally and
642 globally, giving a general indication of a successful mixing of xenon in the bulk liquid argon.

643 The X-ARAPUCA detectors data show an increasing light output with every doping, that
644 anyway appears to approach saturation around 16 ppm of xenon. This effect could be specific to
645 our particular set-up and mixture of Ar-Xe-N₂. One of the two detectors is only sensitive to xenon
646 light, whereas the second is fully sensitive to both wavelengths. The ratio of the light collected
647 by the two sensors testifies that the excitation energy is indeed transferred from argon to xenon.
648 Distinguishing between fast and slow component of the original argon light allows confirming that
649 the energy transfer is happening on the meta-stable triplet state of argon excimer Ar₂*; on the other
650 hand, an unexpected drop in the argon fast component is observed as soon as the first ppm's of
651 xenon are introduced. Data suggest a good stability of the light output in the short-to-mid term (few
652 weeks) after the doping operations were concluded.

653 The ProtoDUNE PDS can yield information on the global detector scale. Data from the two
654 halves of the detector and from different photosensors show behaviours in reasonable agreement,
655 again demonstrating an increase in the number of collected photons, with increasing dopant concen-
656 tration, that anyways reaches a value in line with that obtained from pure argon, before the nitrogen
657 contamination. Studies of light attenuation along the TPC drift distance confirm light recovery
658 with respect to the period with nitrogen contamination, plus demonstrating a relative increase in
659 the amount of light collected far away from the photosensors. This effect was expected and it is
660 ascribed to the higher Rayleigh scattering length of 178 nm photons in argon (with respect to 128 nm
661 photons). In general, temporal stability in the signal is confirmed at the global level. A parallel
662 check of the charge signal from the TPC throughout the doping operations hints at no particular
663 interference between the doping and the TPC.

664 These initial results testify an overall success of the xenon doping, despite some open points on
665 the effect of xenon on singlet argon light and the impossibility to perform the test on uncontaminated
666 argon. More analyses and the reconstruction of the argon-xenon interaction model are needed to
667 more precisely characterise the performance of the detector. A similar test was performed on the
668 other DUNE prototype at CERN, then called ProtoDUNE Dual-Phase, and a combined analysis
669 of the two data-sets is planned. However, the first results from ProtoDUNE SP are already very
670 encouraging and allow proceeding with the plan of doping with xenon the second far detector
671 module of DUNE.

672 A Details on xenon injections in ProtoDUNE SP and contaminations

673 Here, a more in depth description of the actual xenon injection procedure in ProtoDUNE-SP is
674 reported. As mentioned in Section 4.2, the xenon injection point is placed along the chimney
675 boil-off re-circulation line, way before the argon condenser, in order to ensure full argon-xenon
676 mixing within the gas flow.

677 In order to precisely control the amount of gas introduced at any step of the doping, xenon bottles
678 were placed on a scale connected to the detector slow control system. A dedicated purification
679 filter (SAES Micro-Torr) was installed on the line, followed by a mass flow-meter, calibrated for
680 xenon, and a pressure gauge. The entire line installed between the xenon bottle and the connection
681 with the argon re-circulation system was kept under vacuum by a separate pumping system. Xenon
682 pressure, flow and bottle weight were continuously recorded by the slow control system. Figure 22
683 illustrates the xenon injection set up.

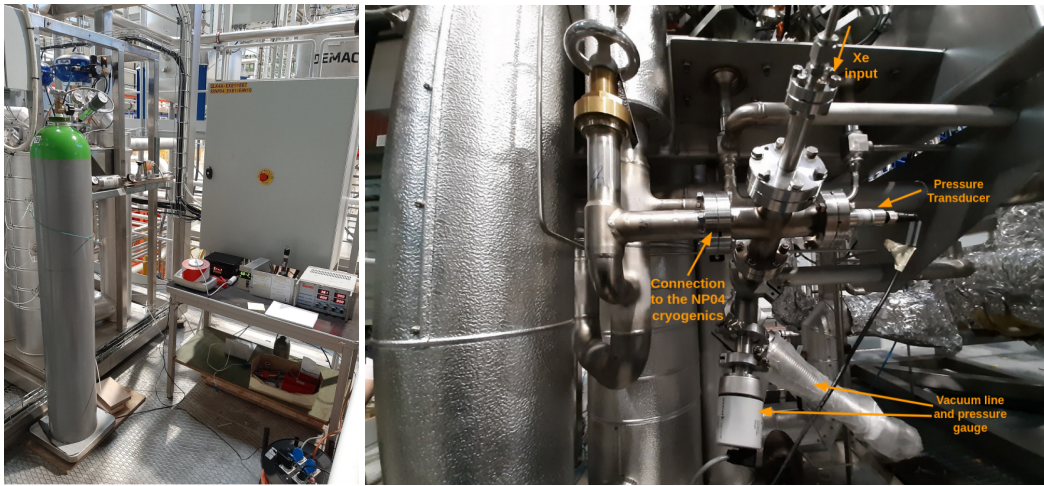


Figure 22: Left: the xenon bottle on the scale connected to the gas purifier, the mass flow-meter and the injection line. Right: the UHV injection line equipped with vacuum/pressure monitoring devices and connected to the NP04 gas circulation system.

684 The doping was performed with three different bottles of xenon. The first one (containing
685 about 3 kg of gas) was rated with a purity grade 5.0³, without any specifications on upper limits
686 on fluorinated compounds. However, during the first injection, a sizable degradation of the free
687 electron lifetime was recorded within the LArTPC, as shown in Figure 23.

688 As a consequence, xenon injection was stopped and a set of spectrographic/ chromatographic
689 analyses were performed at CERN [40] (internal source). Electro-negative impurities were identified
690 as C₂F₆ (~ 10 ppm value to be confirmed. This should correspond to the total amount of
691 contaminants in a 5.0 grade bottle.) plus traces of SF₆ and CO₂. These compounds, that can be
692 present in xenon at the ppm level as residuals of the distillation process, are known to be highly
693 electro-negative (several orders of magnitude higher than Oxygen [41]), hence they can significantly
694 degrade the free electron lifetime in LAr even at concentrations of few ppt. After this episode, free

³The purity grade refers to the fractional amount of gas in their bottle. 5.0 corresponds to 99.999% of xenon in the bottle.

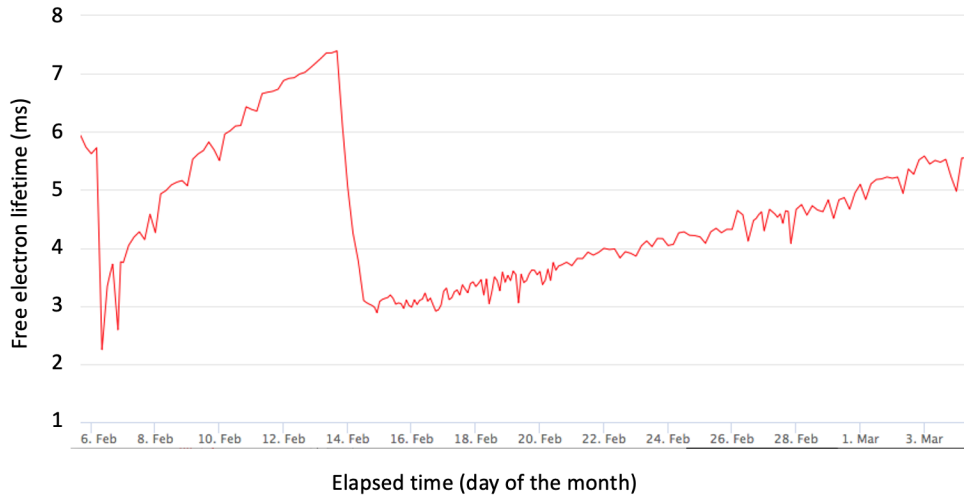


Figure 23: Left: Free electron lifetime measurement in ProtoDUNE-SP performed with dedicated purity monitors. The linear drop recorded around February 13th, coincides with the first xenon injection and is attributed to the presence of fluorinated contaminants in the bottle. The subsequent recovery rate, due to LAr recirculation, is about a factor 8 to 10 slower than in previous recoveries (exemplified in the increase shown prior to the injection). This suggests that the ProtoDUNE purifiers can absorb fluorinated compounds, though with a factor ~ 10 lower efficiency, with respect to oxygen.

695 electron lifetime in ProtoDUNE SP slowly recovered with a time constant of ~ 30 days, indicating
 696 that the purifiers are able to absorb fluorinated compounds, albeit with an efficiency about 10 times
 697 lower than that for oxygen.

698 Two additional xenon bottles (containing about 17.5 kg each) were then acquired, rated with
 699 a purity grade of 5.5 and a specified SF₆ content certified by the producer to be lower than 20 ppb
 700 (following standard procedures set by CERN for the ATLAS and ALICE experiments). No sizable
 701 electron lifetime degradation was observed during the subsequent injections with this higher purity
 702 xenon.

703 References

- 704 [1] C. Rubbia, “The liquid-argon time projection chamber: a new concept for neutrino detectors”,
 705 Technical Report CERN-EP-INT-77-8, CERN, Geneva, 1977.
- 706 [2] S. Amerio et al., “Design, construction and tests of the ICARUS T600 detector”, *Nuclear Instruments*
 707 *and Methods in Physics Research Section A: Accelerators, Spectrometers, Detectors and Associated*
 708 *Equipment* **527** (2004), no. 3, 329–410, doi:<https://doi.org/10.1016/j.nima.2004.02.044>.
- 709 [3] R. Acciarri et al., “Design and construction of the MicroBooNE detector”, *Journal of*
 710 *Instrumentation* **12** (feb, 2017) P02017–P02017, doi:[10.1088/1748-0221/12/02/p02017](https://doi.org/10.1088/1748-0221/12/02/p02017).
- 711 [4] C. Anderson et al., “The ArgoNeuT detector in the NuMI low-energy beam line at fermilab”, *Journal*
 712 *of Instrumentation* **7** (oct, 2012) P10019–P10019, doi:[10.1088/1748-0221/7/10/p10019](https://doi.org/10.1088/1748-0221/7/10/p10019).

- 713 [5] C. E. Aalseth et al., “Darkside-20k: A 20 tonne two-phase LAr TPC for direct dark matter detection
714 at LNGS”, *The European Physical Journal Plus* **133** (2018), no. 3, 131,
715 [doi:10.1140/epjp/i2018-11973-4](https://doi.org/10.1140/epjp/i2018-11973-4).
- 716 [6] B. Abi et al., “Volume I. introduction to DUNE”, *Journal of Instrumentation* **15** (aug, 2020)
717 T08008–T08008, [doi:10.1088/1748-0221/15/08/t08008](https://doi.org/10.1088/1748-0221/15/08/t08008).
- 718 [7] B. Abi et al., “Volume IV. the DUNE far detector single-phase technology”, *Journal of*
719 *Instrumentation* **15** (aug, 2020) T08010–T08010, [doi:10.1088/1748-0221/15/08/t08010](https://doi.org/10.1088/1748-0221/15/08/t08010).
- 720 [8] B. Abi et al., “Supernova neutrino burst detection with the deep underground neutrino experiment”,
721 *The European Physical Journal C* **81** (2021), no. 5, 423,
722 [doi:10.1140/epjc/s10052-021-09166-w](https://doi.org/10.1140/epjc/s10052-021-09166-w).
- 723 [9] S. Kubota, M. Hishida, M. Suzuki, and J. Ruan(Gen), “Liquid and solid argon, krypton and xenon
724 scintillators”, *Nuclear Instruments and Methods in Physics Research* **196** (1982) 101–105.
- 725 [10] M. Suzuki, M. Hishida, J. Ruan(Gen), and S. Kubota, “Light output and collected charge in
726 xenon-doped liquid argon.”, *Nuclear Instruments and Methods in Physics Research* **A327** (1993)
727 67–70.
- 728 [11] M. Hofmann et al., “Ion-beam excitation of liquid argon.”, *The European Physics Journal* **C73** (oct,
729 2013) 2618, [doi:10.1140/epjc/s10052-013-2618-0](https://doi.org/10.1140/epjc/s10052-013-2618-0).
- 730 [12] C. Wahl et al., “Pulse-shape discrimination and energy resolution of a liquid-argon scintillator with
731 xenon doping.”, *Journal of Instrumentation* **9** (2014) P06013,
732 [doi:10.1088/1748-0221/9/06/P06013](https://doi.org/10.1088/1748-0221/9/06/P06013).
- 733 [13] D. Akimov et al., “Fast component re-emission in xe-doped liquid argon.”, *Journal of*
734 *Instrumentation* **14** (sep, 2019) P09022, [doi:10.1088/1748-0221/14/09/P09022](https://doi.org/10.1088/1748-0221/14/09/P09022).
- 735 [14] D. Collaboration et al., “Design, construction and operation of the protodune-sp liquid argon tpc”,
736 [arXiv:2108.01902](https://arxiv.org/abs/2108.01902).
- 737 [15] B. Abi et al., “First results on ProtoDUNE-SP liquid argon time projection chamber performance
738 from a beam test at the CERN neutrino platform”, *Journal of Instrumentation* **15** (dec, 2020)
739 P12004–P12004, [doi:10.1088/1748-0221/15/12/p12004](https://doi.org/10.1088/1748-0221/15/12/p12004).
- 740 [16] Aprile, E. et al., “The xenon1t dark matter experiment”, *Eur. Phys. J. C* **77** (2017), no. 12, 881,
741 [doi:10.1140/epjc/s10052-017-5326-3](https://doi.org/10.1140/epjc/s10052-017-5326-3).
- 742 [17] D. Akerib et al., “The large underground xenon (lux) experiment”, *Nuclear Instruments and Methods*
743 *in Physics Research Section A: Accelerators, Spectrometers, Detectors and Associated Equipment*
744 **704** (2013) 111–126, [doi:https://doi.org/10.1016/j.nima.2012.11.135](https://doi.org/10.1016/j.nima.2012.11.135).
- 745 [18] T. Doke and K. Masuda, “Present status of liquid rare gas scintillation detectors and their new
746 application to gamma-ray calorimeters”, *Nuclear Instruments and Methods in Physics Research*
747 *Section A: Accelerators, Spectrometers, Detectors and Associated Equipment* **420** (1999), no. 1,
748 62–80, [doi:https://doi.org/10.1016/S0168-9002\(98\)00933-4](https://doi.org/10.1016/S0168-9002(98)00933-4).
- 749 [19] M. Babicz et al., “A measurement of the group velocity of scintillation light in liquid argon”,
750 [doi:10.1088/1748-0221/15/09/p09009](https://doi.org/10.1088/1748-0221/15/09/p09009).
- 751 [20] K. Majumdar and K. Mavrokoridis, “Review of liquid argon detector technologies in the neutrino
752 sector”, *Applied Sciences* **11** (2021), no. 6, [doi:10.3390/app11062455](https://doi.org/10.3390/app11062455).
- 753 [21] A. Neumeier et al., “Intense vacuum ultraviolet and infrared scintillation of liquid ar-xe mixtures”,
754 *EPL (Europhysics Letters)* **109** (jan, 2015) 12001, [doi:10.1209/0295-5075/109/12001](https://doi.org/10.1209/0295-5075/109/12001).

- 755 [22] A. Buzulutskov, “Photon emission and atomic collision processes in two-phase argon doped with
756 xenon and nitrogen.”, *Europhysics Letters* **17** (mar, 2017) 39002,
757 [doi:10.1209/0295-5075/117/39002](https://doi.org/10.1209/0295-5075/117/39002).
- 758 [23] R. Acciarri et al., “Effects of nitrogen contamination in liquid argon”, *Journal of Instrumentation* **5**
759 (jun, 2010) P06003–P06003, [doi:10.1088/1748-0221/5/06/p06003](https://doi.org/10.1088/1748-0221/5/06/p06003).
- 760 [24] B. Howard et al., “A Novel Use of Light Guides and Wavelength Shifting Plates for the Detection of
761 Scintillation Photons in Large Liquid Argon Detectors”, *Nucl. Instrum. Meth.* **907** (2018) 9–21,
762 [doi:10.1016/j.nima.2018.06.050](https://doi.org/10.1016/j.nima.2018.06.050), [arXiv:1710.11233](https://arxiv.org/abs/1710.11233).
- 763 [25] L. Bugel et al., “Demonstration of a Lightguide Detector for Liquid Argon TPCs”,
764 [arXiv:1101.3013](https://arxiv.org/abs/1101.3013).
- 765 [26] Z. Moss et al., “A Factor of Four Increase in Attenuation Length of Dipped Lightguides for Liquid
766 Argon TPCs Through Improved Coating”, [arXiv:1604.03103](https://arxiv.org/abs/1604.03103).
- 767 [27] A. Machado and E. Segreto, “ARAPUCA a new device for liquid argon scintillation light detection”,
768 *Journal of Instrumentation* **11** (feb, 2016) C02004–C02004,
769 [doi:10.1088/1748-0221/11/02/c02004](https://doi.org/10.1088/1748-0221/11/02/c02004).
- 770 [28] A. Machado et al., “The X-ARAPUCA: an improvement of the ARAPUCA device”, *Journal of*
771 *Instrumentation* **13** (apr, 2018) C04026–C04026, [doi:10.1088/1748-0221/13/04/c04026](https://doi.org/10.1088/1748-0221/13/04/c04026).
- 772 [29] E. Segreto et al., “First liquid argon test of the X-ARAPUCA”, *Journal of Instrumentation* **15** (may,
773 2020) C05045–C05045, [doi:10.1088/1748-0221/15/05/c05045](https://doi.org/10.1088/1748-0221/15/05/c05045).
- 774 [30] C. Brizzolari et al., “Enhancement of the x-arapuca photon detection device for the DUNE
775 experiment”, [doi:10.1088/1748-0221/16/09/p09027](https://doi.org/10.1088/1748-0221/16/09/p09027).
- 776 [31] Hamamatsu, “MPCC S13360-2050VE/3050VE/6050VE”,
777 <https://www.hamamatsu.com/eu/en/product/type/S13360-6050VE/index.html>.
- 778 [32] DUNE Collaboration, “The Single-Phase ProtoDUNE Technical Design Report.”, Technical Report
779 FERMILAB-DESIGN-2017-02, Jun, 2017. 165 pages.
- 780 [33] A. Curioni et al., “A regenerable filter for liquid argon purification”, *Nuclear Instruments and*
781 *Methods in Physics Research Section A: Accelerators, Spectrometers, Detectors and Associated*
782 *Equipment* **605** (2009), no. 3, 306–311, [doi:https://doi.org/10.1016/j.nima.2009.04.020](https://doi.org/10.1016/j.nima.2009.04.020).
- 783 [34] T. Heindl et al., “Table-top setup for investigating the scintillation properties of liquid argon”, *Journal*
784 *of Instrumentation* **6** (feb, 2011) P02011–P02011, [doi:10.1088/1748-0221/6/02/p02011](https://doi.org/10.1088/1748-0221/6/02/p02011).
- 785 [35] E. Voirin, “ProtoDUNE LAr Flow Simulation- Impurity field and Charge Density.”, Technical Report
786 DUNE DocDB Doc # 928, Jun, 2019.
- 787 [36] M. Morháč et al., “Background elimination methods for multidimensional coincidence γ -ray spectra”,
788 *Nuclear Instruments and Methods in Physics Research Section A: Accelerators, Spectrometers,*
789 *Detectors and Associated Equipment* **401** (1997), no. 1, 113–132,
790 [doi:https://doi.org/10.1016/S0168-9002\(97\)01023-1](https://doi.org/10.1016/S0168-9002(97)01023-1).
- 791 [37] GERDA Collaboration, “Improvement of the energy resolution via an optimized digital signal
792 processing in gerda phase i”, *The European Physical Journal C* **75** (Jun, 2015) 255,
793 [doi:10.1140/epjc/s10052-015-3409-6](https://doi.org/10.1140/epjc/s10052-015-3409-6).
- 794 [38] A. Neumeier et al., “Attenuation of vacuum ultraviolet light in pure and xenon-doped liquid argon
795 —an approach to an assignment of the near-infrared emission from the mixture”, *EPL (Europhysics*
796 *Letters)* **111** (jul, 2015) 12001, [doi:10.1209/0295-5075/111/12001](https://doi.org/10.1209/0295-5075/111/12001).

- 797 [39] D. Adams et al., “The ProtoDUNE-SP LArTPC electronics production, commissioning, and
798 performance”, *Journal of Instrumentation* **15** (jun, 2020) P06017–P06017,
799 [doi:10.1088/1748-0221/15/06/p06017](https://doi.org/10.1088/1748-0221/15/06/p06017).
- 800 [40] M. Corbetta, R. Guida, and B. Mandelli, “Gas chromatograph and mass spectrometer analysis of
801 Xenon bottles used by the ProtoDUNE Experiment.”, Technical Report CERN EP-DT-FS, Mar, 2020.
- 802 [41] G. Bakale, U. Sowada, and W. F. Schmidt, “Effect of an electric field on electron attachment to sulfur
803 hexafluoride, nitrous oxide, and molecular oxygen in liquid argon and xenon.”, *The Journal of*
804 *Physical Chemistry* **80** (nov, 1976) 2556–2559, [doi:10.1021/j100564a006](https://doi.org/10.1021/j100564a006).